DLR

universität
uulm

Simulation of Phase Errors in Interferometric SAR Systems

Master's Thesis

Tanya Gupta

November 2022

Supervisor:	**Dr.-Ing. Josef Mittermayer**
1. Examiner:	**Prof. Dr.-Ing. Christian Waldschmidt**
2. Examiner:	**Prof. Dr.-Ing. Klaus Dietmayer**

Institute of Microwave Engineering
Ulm University

Declaration

I declare that I performed the presented research thesis

Simulation of Phase Errors in Interferometric SAR Systems

myself and that I wrote the thesis myself. Any additional sources of information have been duly identified and referenced. Further, I have regarded the rules of scientific work of the Ulm University.

Ulm, Monday 7$^{\text{th}}$ November, 2022

Tanya Gupta

Acknowledgements

Contents

1 Introduction

1.1 Motivation

SAR interferometry is a well-established radar remote sensing technique to measure the Earth topography on a global scale. For this, two complex-valued SAR images are acquired over the same scene from slightly different view angles. The two images are then combined into a so-called SAR interferogram by complex conjugate multiplication. The phase of each pixel in this complex-valued interferogram is related to the topography, and one can reconstruct a digital elevation model of the imaged scene out of the interferometric data. The accuracy of this height reconstruction is, however, limited by several factors. One important factor is the signal-to-noise ratio in the individual SAR images. This noise is typically modeled by mutually uncorrelated white noise that is added to the individual SAR images. For typical spaceborne SAR systems, it turns out that this noise leads to a high variance of the interferometric phase of each pixel in the complex-valued interferogram, which prevents the generation of an accurate digital elevation model. To overcome this problem, the interferograms are locally averaged by a lowpass (e.g. boxcar) filter before extracting the interferometric phase. Another approach with similar performance generates multiple low-resolution SAR images by dividing the synthetic aperture into shorter apertures, forms then for each an interferogram, and finally averages these interferograms. This so-called multi-looking technique is well suited to reduce the variance of the interferometric phase errors and closed-form expressions are available in the literature of this thesis which relate analytically the noise level (via an intermediate parameter, the so-called interferometric coherence) to the probability density function of the interferometric phase error. An implicit assumption in these analytic expressions is the assumption that the additive noise is independent among neighboring pixels in the interferogram. However, until now, the quality of an interferogram has been only assessed for height error predictions. In practice, phase variations need to be accounted for, too, because the height variations along the scene's horizontal dimensions cause interferometric phase variations that are not perceivable as these high phase fluctuations destroy the phase. The goal of this thesis is to obtain a better understanding of the phase error statistics of interferometric SAR images. For this, SAR image and interferometric processing have been thoroughly analyzed in regard to interferometric phase errors by means of simulated SAR data that is later analyzed with different error reduction techniques. Furthermore, a new parameter called Maximum detectable Frequency of Phase Change (MFPC) is proposed as a quality determinant that gives information about the resolvable phase changes i.e. phase variations in an interferogram.

1.2 Outline

The work in this thesis is structured in the following manner:

- **Chapter 2:** This chapter gives an introduction to the fundamentals of Synthetic Aperture Radar (SAR), its working principle, and geometry. The mathematical description is provided for important parameters of SAR like azimuth and range resolution, backscatter coefficient, and pulse repetition frequency (PRF) are discussed following the introduction of SAR

interferometry. The phenomenon of speckle noise, which arises due to coherent imaging in SAR is mentioned.

- **Chapter 3:** In this chapter, the relation between the topographical phase and height measurement is established. The SAR image statistics regarding intensity, phase, and power spectral density are assessed. The quality factor of interferogram i.e. coherence is discussed and the relation between phase errors and coherence is demonstrated using simulations.

- **Chapter 4** This chapter discusses in detail the image and interferometric processing of an interferometric SAR image pair. The influence of antenna pattern has been studied and supported by simulations. And finally, results have been demonstrated concerning the individual processing steps.

- **Chapter 5:** In this chapter, different phase error reduction methods have been analyzed and compared by extending the simulations from Chapter 4. Finally, a new quality factor for interferometric performance has been proposed that measures the Maximum detectable Frequency of Phase Change (MFPC) in an interferogram.

- **Chapter 6:** This chapter concludes the work by giving a summary of the work and key observations are presented. Additionally, the future scope of work that can be based on this thesis is discussed.

2 Synthetic Aperture Radar Fundamentals

Synthetic Aperture Radar (SAR) interferometry is a renowned remote sensing technique that makes robust use of space-borne radar sensors to perform continuous earth monitoring with highly peculiar technology by leveraging phase information present in the images for computing topographical models of the planet.

This chapter presents an explanation of Synthetic Aperture Radar fundamentals. Firstly, the working principle and geometry of the radar will be demonstrated in which important radar parameters like incidence angle, range resolution, and azimuth resolution will be discussed. Furthermore, important steps in the SAR processing method will be discussed followed by the acquisition modes of SAR. The phenomenon of speckle noise that governs the quality of the SAR image will be discussed in brief in the later sections. The focus point of this thesis will be the concept of SAR interferometry (InSAR) which will be introduced along with its geometrical configurations. While Digital Elevation Model (DEM) construction is the most successful product of InSAR, it has some other important applications like climate monitoring and ocean monitoring that will be mentioned in brief in the last sections and some important missions will also be stated that reinforce the importance of extensive research in the field of InSAR for remote sensing applications.

2.1 Synthetic Aperture Radar

Synthetic Aperture Radar is a high-resolution radar imaging technique used in remote sensing. Its weather-independent operational capabilities make it unique and the most optimal solution for applications like geosciences, climate and environmental research, mapping of earth topography, and planetary research.

In 1978, NASA launched SEASAT [1], one of the first SAR satellites with the goal of global ocean monitoring. It provided a detailed map of the earth's surface, and the scientific community realized its potential which paved the way for advanced research and development in SAR processing.

In the initial phases, the SAR data was processed by optical processing techniques using diffraction gratings to get focused images. But the optical processing posed several constraints and restrictions like process automation as the lenses had to be aligned with great precision. Gradually, with the technical development, those raw images which look like random noise started to be processed using digital signal processing to yield significant phase information [2].

A typical radar installed on a moving platform transmits electromagnetic radiation in the direction of the ground to be observed and the received backscatter from the illuminated region carrying information such as surface properties of the scene is further exploited to get desired amplitude and phase information. The transmitting and the receiving antenna can be the same or different depending on the type of radar i.e, monostatic or bistatic radar. Since it is an active microwave system, it is not affected by daylight, cloud cover, etc. which is its main advantage over optical imaging systems that are restricted by the availability of sunlight. Additionally, the penetration capabilities of different wavelengths allow for a range of mapping and monitoring applications. For example, ocean and agricultural monitoring are frequently done in the L-band

and X-band, and P-band is used for biomass estimation, whereas glaciology is often performed in the ku-band [3]. The scattering property of the radar radiation depending on the frequency reveals more additional information about the surface characteristics than what an optical image can produce. The longer wavelength implicates deeper surface penetration. The raw image that resembles a hologram has to be extensively processed to obtain meaningful phase information. A conventional real aperture radar uses a beam-scanning antenna where the antenna size has to be large to obtain higher resolution images. The term "synthetic aperture" is a clever solution to the impractically large size of the antenna for better resolution. In SAR, the Doppler frequency in flight direction of the moving radar is utilized in such a way that the sequentially received radiation by the antenna creates a much longer virtual aperture, giving high-resolution images with an antenna of a physically shorter aperture [3].

2.2 Working Principle and Geometry

The radar sensor is installed on an airborne platform moving in a straight direction called *azimuth* and the direction orthogonal to the flight path is called *slant range* or *range* and the swath width is the radar footprint range along the ground also known as *ground range* [3]. And thus the raw image is obtained in two dimensions i.e, range and azimuth. The side-looking geometry of SAR is depicted in Fig. 2.1. Θ_a gives the radar beamwidth and v gives the radar velocity in azimuth direction [3].

It can be seen from Fig. 2.1 that the radar sensor is continuously moving emitting successive
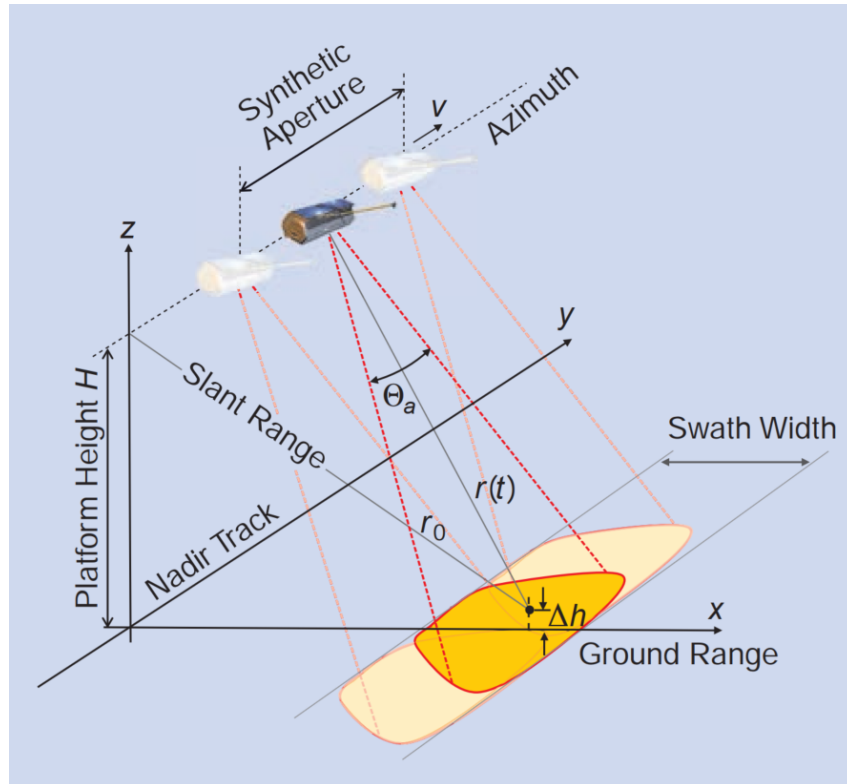

Fig. 2.1: SAR acquisition geometry - The radar flies in azimuth direction and transmits a signal in range direction [3].

radar pulses. The backscatter echo from the target is collected throughout the duration as long as the target remains in sight. The distance corresponding to this *integration time* determines the length of "synthetic" aperture [3]. It is the time in which the target remains within the usable beamwidth of illumination, which is usually $3\,\mathrm{dB}$ beamwidth. The increase in virtual length of the aperture dictates improved resolution.

The movement of the radar along the flight path causes a Doppler effect as a result of continuously changing range. As the radar moves in direction of the target, the range distance between the sensor and target decreases causing frequency of the received signal to increase, and as it moves away, the distance increases again, and frequency of the received signal decreases. The relative distance gives rise to Doppler frequency shift. This Doppler frequency shift makes it possible to separate the targets located at different positions on the ground by frequency filtering [3].

2.2.1 SAR Parameters

The SAR imaging process is characterized by several parameters that govern the system performance. Some of the important parameters are discussed below:

- **Incidence angle:** The incidence angle influences the behavior of the radar backscatter information. The incidence angle θ as depicted in Fig. 2.2 is described as the angle between the flat ground plane and the incident radar radiation. θ is a function of radar height. The points on the scattering object have different heights, and therefore, from each point the radar height is different. This causes the geometry of the image to change for every point. However, the earth's surface is not flat. The surface normal of scatterer is shifted by the local inclination and the respective angle is called local incidence angle θ_l [4].
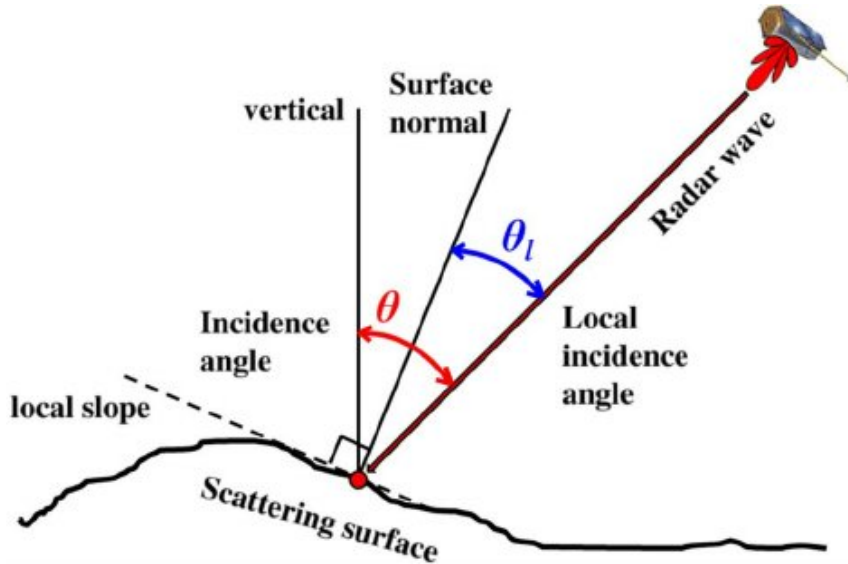

Fig. 2.2: Illustration of incidence angle θ and local incidence angle θ_l [4].

- **Azimuth resolution:** Azimuth resolution of a SAR image is determined by the length of the synthetic aperture L during acquisition. The azimuth resolution is derived by [3].

According to Fig. 2.1, the synthetic aperture length L can be given by:

$$L = \frac{\lambda r_o}{d}, \tag{2.2.1}$$

where r_o is the range of closest approach and d is the azimuth antenna length. As the aperture length increases, the antenna beam Θ_a from sensor to target becomes narrower and the resolution becomes better. The azimuth resolution is given as:

$$\theta_a = \frac{\lambda r_o}{2L} = \frac{d}{2}. \tag{2.2.2}$$

The factor 2 is due to the two-way travel path of the radiation (transmission and reception).

- **Range resolution:** The slant range resolution is defined as the minimum resolvable distance between two scattering objects on the ground such that the objects can be distinguished. It is related to the transmitted pulse shape and is independent of the antenna dimensions.

  From the basic radar principles, it is known that the shorter pulse gives high slant range resolution according to the following relation:

$$\theta_r = \frac{c_o T_p}{2}, \tag{2.2.3}$$

where c_o is the speed of light and T_p is pulse width.

In airborne radars, a frequency sweep signal that uses linear frequency modulation also known as a chirp signal is used whose energy is spread over the entire bandwidth and by using a matched filter, a compressed pulse with higher peak power is obtained and thus better SNR is achieved [5]. The radar transmit pulse is given by:

$$g(t) = A(t)\cos(2\pi f_o \tau + \pi k_r \tau^2), \tag{2.2.4}$$

where f_o is the center frequency and k_r is the rate of increasing/decreasing frequency known as chirp rate. The slant range resolution dependent on the signal bandwidth B_s can be stated as [3]:

$$\theta_r = \frac{c_o}{2B_s}. \tag{2.2.5}$$

From equation 2.2.5, it can be observed that resolution improves with the increasing bandwidth. But larger bandwidth also indicates higher system noise which in turn degrades system performance. Therefore, a trade-off has to be attained between system bandwidth and SNR.

The ground range resolution θ_g is determined by the incidence angle θ as can be observed from the Fig. 2.3.

The relation between the slant range and ground range resolution can be given as follows:

$$\theta_g = \frac{\theta_r}{\sin\theta}. \tag{2.2.6}$$

It is interesting to note that the chirp signal is only used in range whereas in azimuth, the frequency is modulated due to the movement of the radar in azimuth direction. This
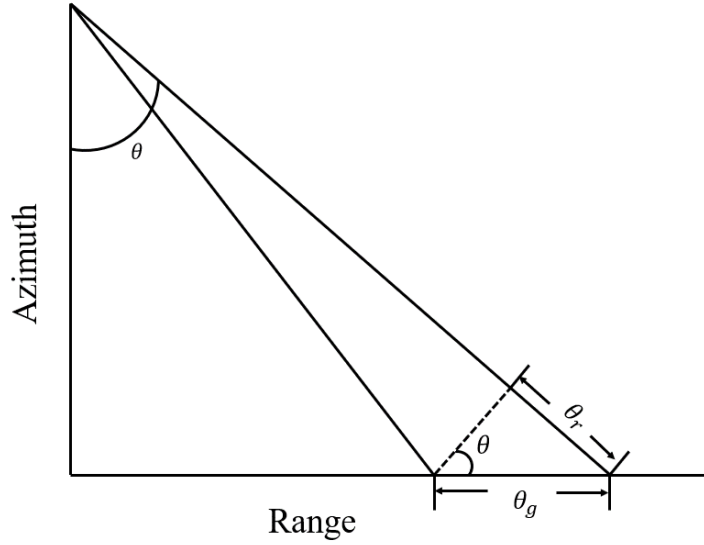
Fig. 2.3: Illustration of slant range and ground range resolution, θ_r and θ_g respectively.

azimuth modulation is a good approximation also of a chirp signal.

- **Backscatter coefficient:** The reflected signal from the ground is characterized by the intensity of each pixel. The radar backscatter coefficient is essentially the normalized radar cross-section. It is a measure of energy reflected towards the radar with respect to the energy radiated isotropically [6]. The positive backscatter coefficient indicates that energy is radiated in the direction of the radar and intuitively negative backscatter indicates that energy is radiated away from the radar. The backscatter is very high for rough surfaces or terrains such as urban areas and considerably lower for smooth surfaces such as roads and standing water bodies. It is also driven by surface parameters such as scatterer structure and its dielectric constant. The backscatter coefficient σ_o is given as:

$$\sigma_o(dB) = 10 \log_{10}(E), \tag{2.2.7}$$

where, E is the ratio of backscatter signal energy towards the radar sensor to the signal energy radiated isotropically.

- **PRF:** While the radar is moving, it transmits chirp pulses. These pulses are transmitted priodically at the Pulse Repetition Frequency (PRF) and the corresponding time period between the pulses is called Pulse Repetition Interval (PRI) [3]. To avoid aliasing, the PRF should satisfy the nyquist criterion. A higher PRF improves the azimuth resolution but limits the swath width. It goes along with a smaller antenna, and a higher azimuth bandwidth requires then a higher PRF. In the azimuth direction, multiple receive channels can facilitate achieving a higher PRF wihtout circumscribing the swath width [7].

2.2.2 Geometrical Effects

The uneven surface of the earth makes the SAR image formation a complex process. Based on signal interaction with the scattering surface, geometrical distortions are easily observable in the image signal. These distortions can be introduced during the signal processing or can be a result of anomalies in the radar perceiving geometry. Some of these geometric distortions are described below:

- **Shadowing:** As suggested by name, shadowing in SAR is similar to the optical shadowing phenomenon. It is typically caused by the obstruction of a surface by another object that restricts the radar signal from reaching the surface. As a result, there is no backscatter carrying surface information, and the area is represented by a dark patch. It usually occurs in forests or mountainous regions.

- **Layover:** This effect occurs in regions with higher terrain differences as signals reflected from different heights reach at different times.

- **Foreshortening:** It is an effect that causes a change in the perceived size of objects with similar surface characteristics at different ranges.

These geometric distortions are demonstrated in Fig. 2.4.
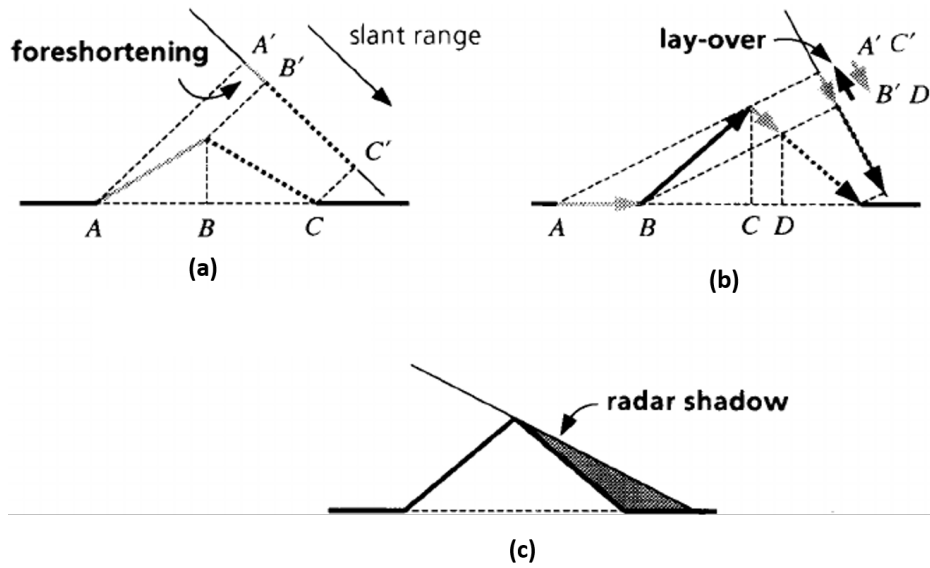
Fig. 2.4: Illustration of geometrical distortions in a SAR image caused by sensor viewing geometry: Foreshortening, Layover and, Shadowing [6].

[8] gives a detailed overview of other geometric distortions such as due to Earth's curvature and rotation, system characteristics, and ground-range distortions that dramatically impact SAR image quality.

2.3 SAR Processing

The raw SAR signal looks like just noise in range and azimuth direction however, it is principally the useful signal. The raw backscatter signal requires extensive processing to reveal valuable

information. The raw signal is processed to form a focused complex SAR image.

After the acquisition, the signal needs to be amplified and down-converted to a baseband signal. After performing signal processing and storing the signal, a focused image is derived. In a conventional method, the focusing of the complex image using a matched filter is implemented in a two-step process: range compression and azimuth compression [9]. During range compression, the range line of the raw data is convolved with a range reference function which is essentially the complex conjugate of the transmitted pulse. After this process, a phenomenon called *range cell migration* occurs in which a target response is shifted to a different resolution cell. A range cell migration correction (RCMC) algorithm based on Envelope Correlation Method is discussed in [10]. After RCMC, azimuth compression is performed with the azimuth reference function dependent on the azimuth position of the sensor as demonstrated in Fig. 2.5. The reference function is multiplied column-wise to the range corrected 2D matrix. And finally, a focused image is produced by taking an inverse Fourier transform of the final product [11]. A SAR image is a 2D matrix of complex signals spread across range and azimuth. It has both phase and amplitude information, and the intensity is derived from the amplitude which is related to the backscatter power.
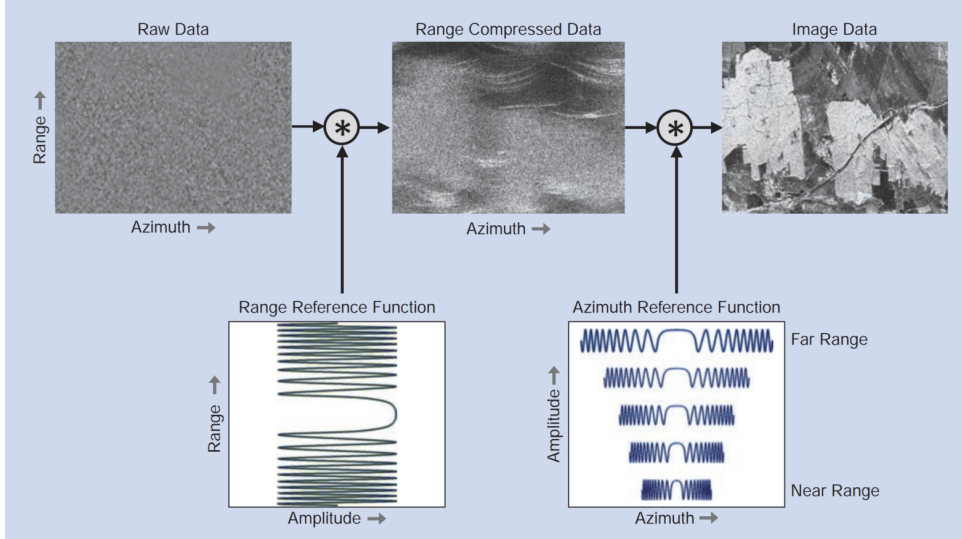

Fig. 2.5: SAR processing steps involving range and azimuth compression and convolution with range and azimuth reference functions as intermediary steps [3].

2.4 SAR Acquisition modes

The radiation beam configuration of the radar can control the operation mode for imaging depending on the application and the surface to be scanned. Different acquisition modes of conventional SAR as shown in Fig. 2.6 are discussed below:

- **Stripmap mode:** This is the fundamental imaging mode in SAR in which the radar constantly sweeps across the area to be imaged forming a strip during the entire illumination time.

- **ScanSAR mode:** The antenna beam is electrically steered in elevation to cover multiple

sub-swaths. The regions are illuminated for a short time by a smaller aperture which worsens the azimuth resolution but allows coverage of a wider swath composed of sub-swaths [12].

- **Spotlight mode:** The azimuth resolution can be improved by extending the illumination time. The antenna is electrically steered to illuminate patches for a longer time and thus improving the resolution.

There are other modes of operation that overcome certain shortcomings at the expense of other parameters. For an instance, to get a wider swath, the azimuth resolution has to be degraded and vice versa.
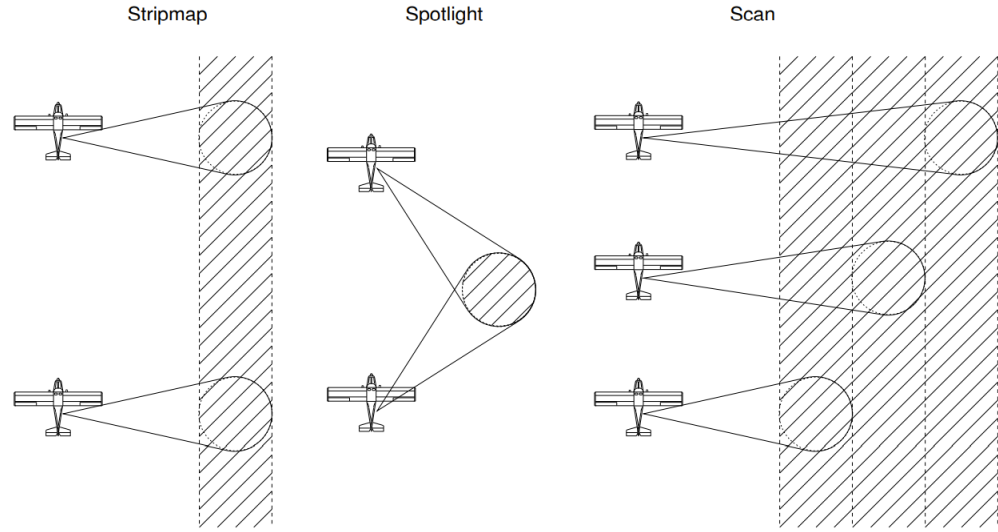

Fig. 2.6: Illustration of SAR acqusition modes: Stripmap mode, Spotlight mode, and ScanSAR mode [12].

2.5 Speckle

Speckle is an interesting phenomenon that occurs as a consequence of coherent imaging of the radar. Although, it is coherent imaging that gives SAR benefits over optical imaging techniques, the same property arises effects that if not compensated for, significantly impact the image quality. Speckle is often misinterpreted as noise but in reality, it is the fluctuation in a signal that is prone to variations caused by many individual scatterers. It can be understood as coherent addition of the backscattered signal. This causes variation in the intensity of the reflected wave and incoherence in the phase of many individual scatterers within a resolution cell due to the rough surface. It is also referred to as granular noise. Fig. 2.7 illustrates the vector addition of randomly distributed pixel intensity [13]. The variation caused due to the speckle effect gives rise to errors in the intensity measurement of a single pixel. Therefore, speckle denoising is an important step in SAR image processing. However, conventional denoising methods cannot be applied to mitigate its effect as granular noise is multiplicative and the traditional denoising methods take into account additive noise. [14] uses log transformation to overcome the limitations of multiplicative noise by transforming it into additive noise which reduces the time and computational complexity. The uncertainty in pixel intensity makes it exceedingly difficult to segregate targets and perform
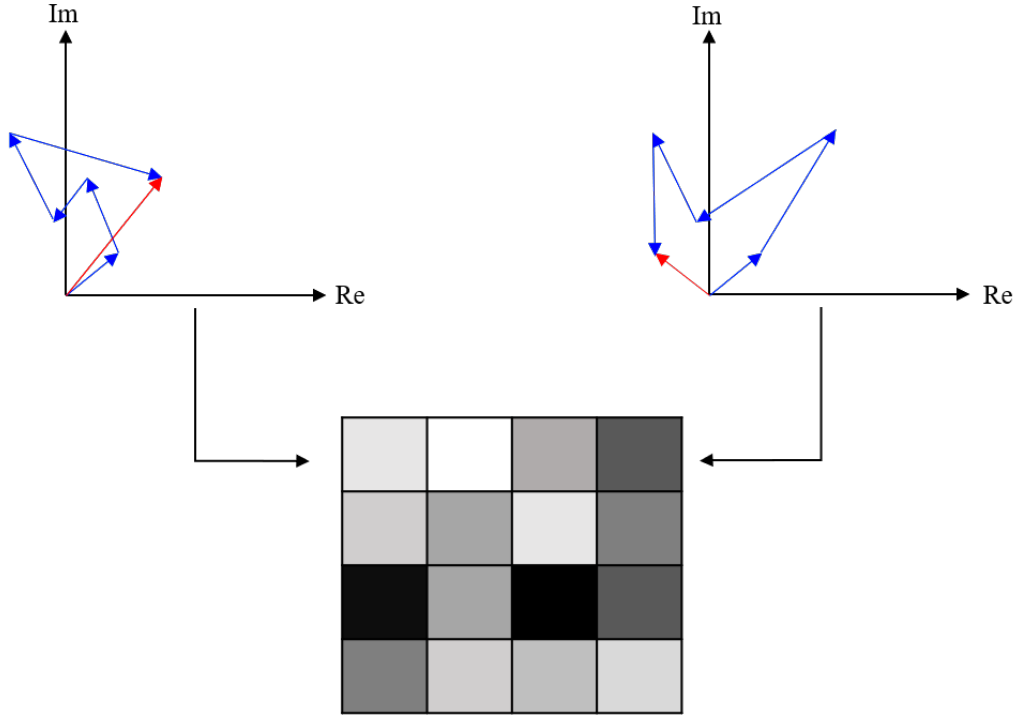
Fig. 2.7: Demonstration of speckle effect that occurs due to constructive and destructive interference of signals from elementary scatterers in the resolution call.

edge detection. To accomplish this, sophisticated techniques are used to minimize this effect. The use of adaptive filters retains the inherent properties of the image whereas adaptive filters average out the entire image causing a loss in the image's natural properties. In later chapters, multilooking technique will be thoroughly investigated which is used for the reduction of speckle noise. Multilooking is an important averaging technique as a possibility to decrease interferometric phase noise where the radar aperture is divided into shorter apertures to take multiple low-resolution images of the same scene that are added incoherently to obtain an image with reduced noise. In SAR image processing, it is used to reduce the speckle noise.

2.6 SAR Interferometry (InSAR)

A SAR image is a complex image that contains phase and amplitude information. This helps in the determination of position and properties of an object but has limited height accuracy due to phase ambiguities in a single image. By obtaining multiple images of the same target area, the phase difference in the images can improve the precision of height determination as a different observation angle generates a phase difference in the images that can provide precise height information. So, the phase information in the two complex SAR images is utilized to measure height with great definitiveness which makes phase a crucial parameter for construction of a DEM of the Earth. Fig. 2.9 shows the SAR image and corresponding interferogram of volcano Kilauea obtained by NASA in 1999 [15][16].

Since the purpose of this thesis is the simulation of the phase errors which can limit the height measurement accuracy, the phase error statistics will be discussed in detail and validated by numerical simulations in the following chapters.

In Across-track Interferometry, there exist two possible configurations. First is the repeat pass interferometry in which the same satellite takes two images of a scene at different times. This facilitates the determination of surface displacements in a scene. In the other configuration called single pass interferometry, two different satellites having flight paths parallel to each other take images of the same scene from a relatively different position with a slightly different look angle. The distance between the satellite flight trajectory is called as *baseline* [17].
The interferometric formation of two satellites is depicted in Fig. 2.8.
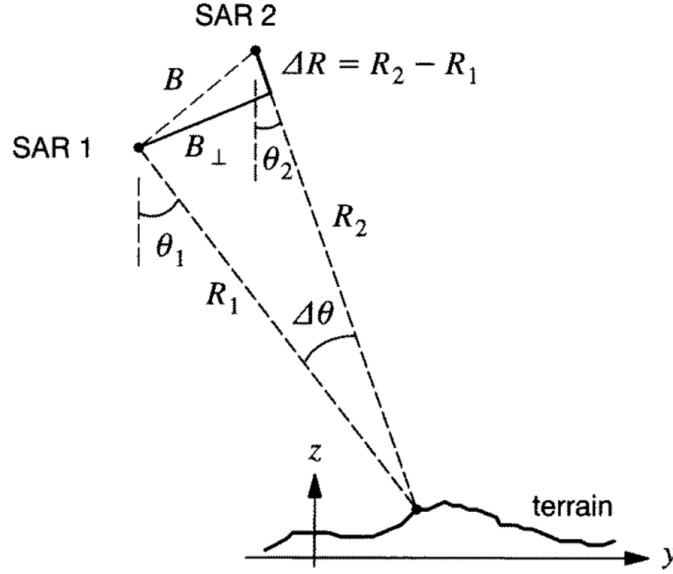

Fig. 2.8: Illustration of InSAR acquisition geometry. R_1 and R_2 are the ranges from the two radar satellites SAR 1 and SAR 2 to the point target on Earth. θ_1 and θ_2 are the look angles of the respective radars. B is the baseline and $B_\perp$ is the effective baseline [17].

According to Fig. 2.8, let us consider, the two complex images taken by SAR1 and SAR 2 are i_1 and i_2. After performing coregistration of the images to align pixels in the corresponding resolution cells of the two images respectively, the complex conjugate multiplication of the two complex images is carried out. This product is called as *interferogram*. An interferogram contains intensity information of the pixels and the phase difference φ between the two interferometric images. The interferogram u can be computed as [17]:

$$i = i_1.i_2^*, \tag{2.6.1}$$

$$i_1 = |i_1|.e^{j\varphi_1}, \tag{2.6.2}$$

$$i_2 = |i_2|.e^{j\varphi_2}, \tag{2.6.3}$$

$$u = |i_1|.|i_2|e^{j\varphi}, \tag{2.6.4}$$

where $|i_1|$ and $|i_2|$ are the magnitudes of reflected energy of the respective images that depend on surface characteristics like roughness and inclination, and φ_1 and φ_2 are the respective phases of the two images that contain the information of distance from the antenna to the point target on the ground. φ is the phase difference of the images i_1 and i_2 called as *interferometric phase*
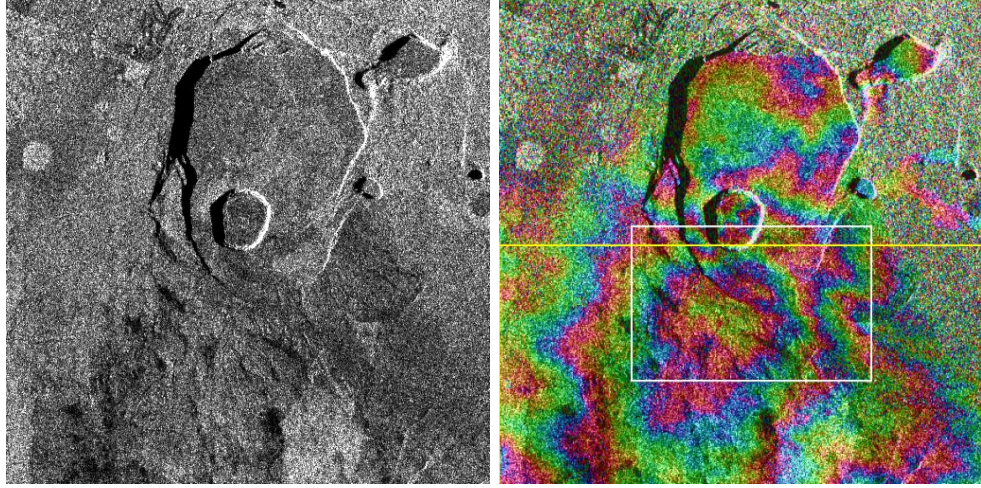
Fig. 2.9: On the left, X-band image of volcano Kilauea by SIR-C/X-SAR, NASA [15]. On the right, Interferogram obtained from the X-band image of Volcano Kilauea by SIR-C/X-SAR, NASA [16].

and can be written as:

$$\varphi = \varphi_1 - \varphi_2. \tag{2.6.5}$$

The interferometric phase and its staistical properties will be demonstrated by numerical simulations in detail in the following chapters.

2.7 Applications and Missions

After the conceptualization of SAR by Carl A. Wiley in 1951, the early development of InSAR happened in the 1980s. In the 1990s, ERS-1 and ERS-2 were major breakthroughs in the InSAR technology that achieved highly precise orbits and required stability. InSAR has been a major success in the mapping of Earth's topography with ultraprecision. The phase information of the interferogram reveals information about the changes in surface properties like deformation, displacement, melting of ice caps and help in monitoring global hazards, climate change, ocean currents, volcanic activity, and land shits in the mountainous regions.

In [18], Didier Massonnet and Thierry Rabaute demonstrated the formation of the Digital Terrain Model by evaluating the interferometric phase by resolving phase unwrapping using Differential Interferometry which as they predicated correctly has vital use cases in risk management applications. Today, climate change is the biggest conundrum that our planet is facing and the monitoring of the glaciers, their response to atmospheric patterns, and resulting displacement and motion are of absolute priority among all scientific communities around the world. In [19], Kwok and Fahnestock used multi-pass interferometry combined with Differential Interferometry to obtain an interferogram containing topography information to obtain relative movement and flow in the glaciers. In [20], the behavior of ice in the West Antarctic ice sheets and subsequent streams is predicted which paves the way for promising models for East Antarctic and Greenland ice models.

InSAR has also demonstrated capabilities of forestry management and water level monitoring as discussed in [21], and [22] respectively. ERS-1 and ERS-2 were the most important Earth Observation Satellite missions of ESA that presented the global DEM [23], and the associated

Missions	ERS-1/2	SRTM	Terra-SAR (X)	Tandem-X (X)
Country	Europe	USA, Europe	Germany	Germany
Year	1991-95	2000	2007	2010
Altitude [km]	790	233	514	515
Frequency [GHz]	5.25	C- 5.25, X- 9.6	9.65	9.65
Polarization	VV	HH, VV	HH, VV	HH, VV
Incidence Angle [deg]	21-26	54	20-55	20-55

Tab. 2.1: List of SAR Missions [28], [29].

multitude of projects contributed to all aspects of remote sensing from oceanography [24] to atmospheric monitoring [25].

TanDEM-X is a highly advanced InSAR mission dedicated to the construction of DEM conforming to HRTI-3 protocols. In a synchronous orbit with TerraSAR-X, the system forms a sophisticated interferogram with a HELIX orbit formation configuration. The potentials and mission concepts of this innovative SAR marvel are comprehensively explained in [26].

In 2022, the world witnessed major consequence of climate change. Extreme temperatures and heat waves were recorded in all regions around the globe. Copernicus Sentinel-3 mission mapped the extreme temperatures in France, Spain, and other European regions confirming the tragically increasing temperatures, and their devastating consequences like wildfires, according to an article published by ESA [27].

Some popular SAR missions are listed in Tab. 2.1.

3 Interferometric SAR (InSAR)

The term interferogram comes from interference and intuitively begets from young's interference idea. The interference between two images of the same scene is mapped in the interferogram and that allows us to understand how the phase of the two complex images is interacting mutually. This phase difference of each pixel in the complex-valued interferogram is related to the terrain of the scene. Consequently, phase errors directly correspond to height measurement errors and it is thus critically important to perform phase error mitigation.

In this chapter, the discussion begins with the interferometric phase definition and properties. A mathematical description of the evaluation of height estimation from phase difference is provided. The nature of the SAR image following the simulation to investigate its behavior in terms of intensity, phase distribution, energy, and power spectral density is discussed. The concept of coherence will be introduced that is strictly related to phase and statistical results with varying parameters will be compared by numerical simulations. Coherence is an important parameter for the underlying phase measure of an image. It is important to note that the predictions will be made in terms of the probability density function and standard deviation. Finally, two methods will be introduced to simulate random Gaussian images with certain coherence to help understand the relation between coherence and phase errors. The emphasis of the findings will exclusively be on the mathematical description of the interferometric phase errors and their statistical properties.

3.1 Interferometric Phase

From, chapter 2, it is already known that equation 2.6.1 generates the interferograms of two complex images i_1 and i_2 out of which crucial phase information can be derived.

The interferometric phase in the images is directly related to the range and a random path shift caused by the point scatterer denoted by φ_{sc_1} and φ_{sc_2} in the two images. In reference to Fig. 2.8, where R_1 and R_2 are the respective slant ranges from the two satellites' antennas and λ is the radar wavelength. Each radar measures the same scene independently with at least one different parameter. The phase of the images considering the shift, according to [17] can be given as:

$$\varphi_1 = -\frac{4\pi}{\lambda}.R_1 + \varphi_{sc_1}, \tag{3.1.1}$$

$$\varphi_2 = -\frac{4\pi}{\lambda}.R_2 + \varphi_{sc_2}. \tag{3.1.2}$$

Using equation 2.6.5, 3.1.1, and 3.1.2, assuming that shift caused by the point scatterer in both the images is identical, the phase difference φ can be written as:

$$\varphi = \frac{4\pi}{\lambda}.\Delta R. \tag{3.1.3}$$

Therefore, the millimeter wavelength precision of phase measurement leads to a highly accurate measurement of the range difference ΔR.

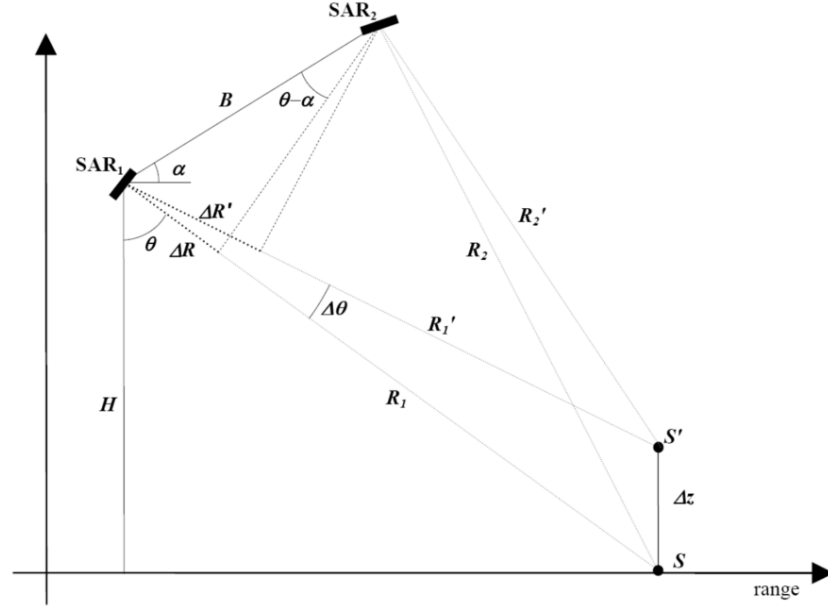Let us consider a scenario where two interferometric radars are observing points S and S'. The

Fig. 3.1: The two radars SAR_1 and SAR_2 are observing the two points S and S' located at different heights with the height difference Δz. R_1, R_2, and R_1', R_2' are the two respective slant ranges from the radars to S and S' [30].

height difference bewteen the two respective positions can be estimated in the following way. The height can be estimated from the phase, and any variation in the height causes a corresponding change in the phase. To investigate height information from interferometric phase, refer to Fig. 3.1. The height estimation is based on the evaluations in [30]. The perpendicular distance between the two radars is related to the baseline projection such that:

$$\Delta R = R_1 - R_2 = B\sin(\theta - \alpha) \tag{3.1.4}$$

ΔR is the range difference due to point S and $\Delta R'$ is the range difference due to point S' and α is the angle between parallel plane and baseline. The interferometric phase w.r.t point S' using equation 3.1.3 can be written as:

$$\varphi' = \frac{4\pi}{\lambda}.\Delta R'. \tag{3.1.5}$$

The change in scatterer height Δz causes a change in the look angle θ as demonstrated in Fig. 3.1. The range difference due to change in height $\Delta R'$ can be written using equation 3.1.4 as a function of the look angle variation in the following way:

$$\Delta R' = B\sin(\theta + \Delta\theta - \alpha). \tag{3.1.6}$$

Using equation 3.1.3, the phase difference $\Delta\varphi$ can be obtained from the height difference Δz such that:

$$\Delta\varphi = \frac{4\pi}{\lambda}.(\Delta R - \Delta R') = \frac{4\pi B}{\lambda}.(\cos(\theta - \alpha)\Delta\theta). \tag{3.1.7}$$

The height H of SAR_1 from the ground can be written as:

$$H = \Delta z + R_1 \cos(\Delta\theta), \tag{3.1.8}$$

Using small-angle approximation,

$$\Delta\theta = \frac{\Delta z}{R_1 \sin\theta}. \tag{3.1.9}$$

Putting the value of look angle difference $\Delta\theta$ in equation 2.6.5, the phase difference is obtained as:

$$\Delta\varphi = \frac{4\pi B}{\lambda R_1 \sin\theta}.(\cos(\theta - \alpha)\Delta z). \tag{3.1.10}$$

Equation 3.1.10 gives the relation between topographical phase and height measurement crucial for DEM construction.

3.2 SAR Image Statistics

The properties of SAR image have significant impact on the interferometric phase properties. In this section, a complex SAR image will be studied by simulations to examine its behavioral properties.

SAR image can be described as a function of range and azimuth where r is range and a is azimuth. The SAR impulse response convolved with the scene reflectivity function gives a complex SAR image. In practical scenarios, the scatterers are considered Gaussian distributed and the respective image pixel is assumed to be a circular Gaussian random variable. The distribution of scatterers in a resolution cell is considered to be homogeneous. The expected image pixel intensity according to [17] is described analytically as:

$$I_p = E[|i(r,a)|^2], \tag{3.2.1}$$

where, $E[.]$ is the expectation value.

The probability density function of the image i is given as [17]:

$$PDF(i) = \frac{1}{\pi I_p} e^{-\dfrac{(Re\{i\})^2 + (Im\{i\})^2}{I_p}}. \tag{3.2.2}$$

The image here is considered to be modeled by uncorrelated additive White Gaussian noise. However, the phase of each pixel does not give us valuable scene information. The scene information is derived from the interferometric phase which is the phase difference of two images.

3.2.1 Simulation of a SAR Image

In this section, a 2D complex SAR image $s(t)$ in the time domain is simulated with dimensions range r and azimuth a typically characterized by circular Gaussian noise to understand the behavior of intensity, phase, and power spectral density of the Gaussian image as demonstrated below. The noise is assumed to be uncorrelated among the neighboring pixels.

The pixel value is assumed to be a complex independent circular Gaussian random variable with standard deviation σ and unit mean μ, as it is a close approximation for natural scatterers like

Parameter	Value
Samples in range and azimuth	512, 8192
PRF	3000 Hz
Azimuth acquisition bandwidth	3000 Hz
Fs	100 MHz
3dB processed bandwidth B_a	3000 Hz
Azimuth sampling interval	0.3 ms
Range sampling interval	5.12 μs
Signal/Noise power (N)	25 dBm = 0.316 V^2
Standard deviation σ	0.397
Mean μ	0

Tab. 3.1: Parameters of complex Gaussian SAR image.

oceans, forests, etc. Note that, in our simulations, only Gaussian scatterers are considered in a resolution cell which implies there are no dominant scatterers [17].

The standard deviation of the samples in the image can be given by real and imaginary parts as follows [31]:

$$\sigma \Rightarrow \sigma_p = \sigma_{Re} = \sigma_{Im} = \sqrt{\frac{E\left[I\right]}{2}} = 0.397 \tag{3.2.3}$$

where, $E\left[I\right]$ is the expectation value of the pixel intensity.

The complex circular Gaussian image of the scene footprint which is essentially Gaussian noise received by the antenna is simulated with the parameters given in Tab. 3.1. Here, PRF is the sampling frequency of the pixels in azimuth and Fs is the sampling frequency of the pixels in range. Noise power N can be defined as noise power per unit frequency bandwidth. Note that, here, azimuth acquisition bandwidth is same as azimuth 3 dB processed bandwidth B_a.

The simulated complex Gaussian image is shown in Fig. 3.2.

To understand the behavior of pixels in a SAR image, we will now study the intensity, phase,
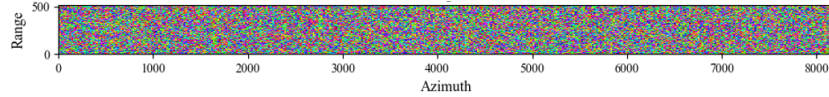
Fig. 3.2: Simulated complex Gaussian SAR image

energy, and power spectral density of the Gaussian signal.

- **Intensity:** The intensity of a signal in time domain can be defined as the power that drops at theoretical unit resistance. The expected image pixel intensity in azimuth profile is constant for all the samples. The azimuth profile is used in simulations because the signal is highly sensitive in azimuth range and concludes valuable statistical measures. Fig. 3.3 demonstrates the process of obtaining azimuth profile of a 2D complex SAR image.

  The signal intensity I of $s(t)$ according to equation 3.2.1 can be written as:

$$I = \left|s(t)\right|^2 \tag{3.2.4}$$

  The intensity profile of the pixels in azimuth profile is depicted in Fig. 3.4. It can be seen that all the pixels have constant intensity of 0.316 V^2. Signal intensity is an important
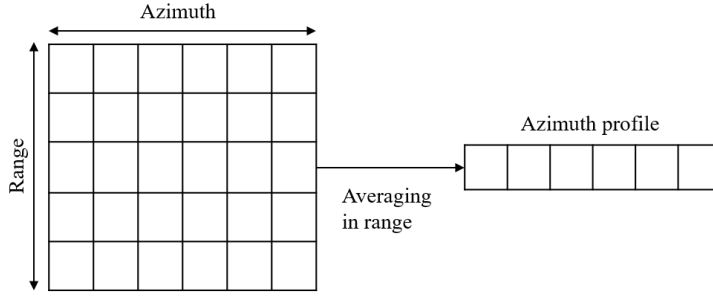
Fig. 3.3: The azimuth profile of a 2D image is obtained by averaging all range lines.

parameter of the received signal as it conveys information about the object properties like roughness, illumination etc.
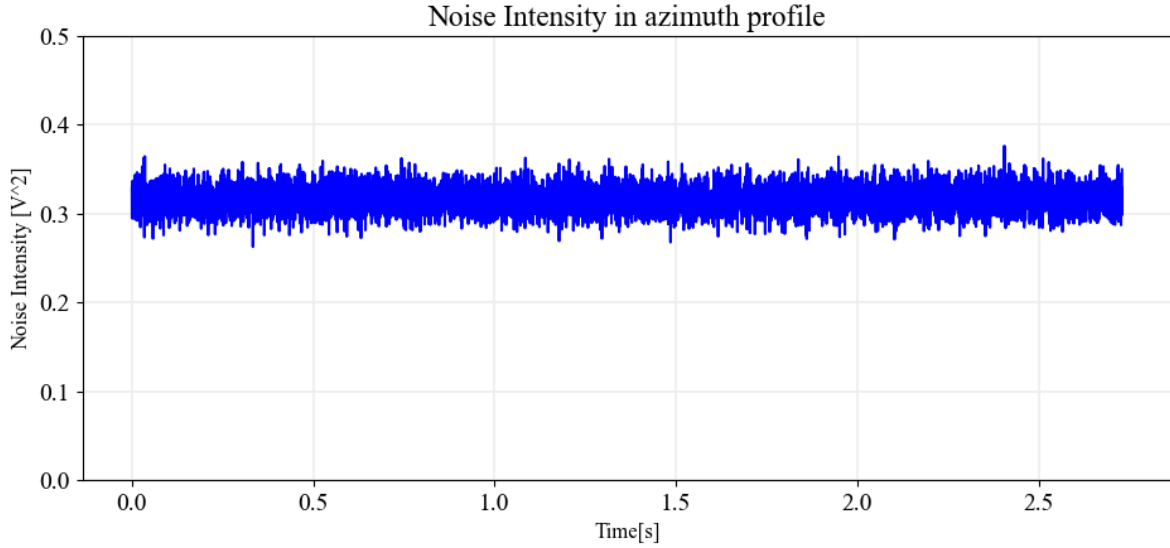

Fig. 3.4: Intensity of the pixels in azimuth profile of SAR image signal $s(t)$.

- **Energy:** The energy per sample is the backscatter energy of each pixel and is obtained by noise intensity in one azimuth sample of duration Δt as depicted in Fig. 3.4 and can be given as:

$$E = N \times \Delta t$$

where, a is the number of samples in azimuth and Δt is the azimuth sampling interval. The average enery per pixel in azimuth profile is shown in Fig. 3.5.

- **Phase:** In previous sections, the importance of phase in SAR image has already been discussed. Although, the phase of the pixel in the signal image carries no relevant information, it is still vital to understand its distribution. The pixel phase is uniformly distributed between intervals $[-\pi, \pi)$. The phase distribution in range and azimuth can be observed from Fig. 3.6 in the left figure and for phase in time, in the right figure. It can be seen, that the summation of white Gaussian noise in real and imaginary parts leads to a uniform distribution.
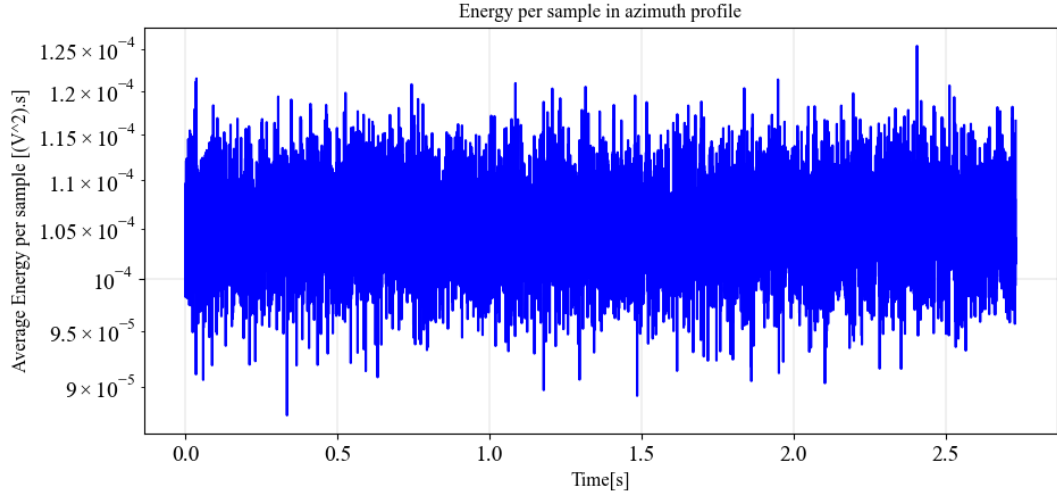
Fig. 3.5: Average energy per pixel sample in azimuth profile of SAR image $s(t)$.
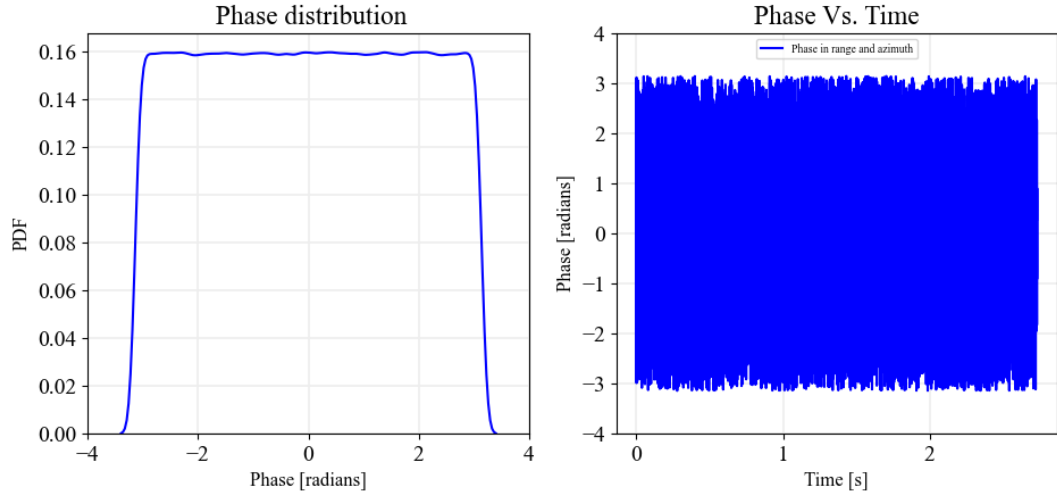

Fig. 3.6: Left: Phase distribution of signal $s(t)$. Right: $s(t)$ in time domain.

- **Power Spectral Density (PSD):** A typical Gaussian SAR image delivers the same average power for all frequencies. Therefore, the PSD N_o of a SAR image has constant power in the entire azimuth bandwidth as the image is modeled by White Gaussian noise and the constant spread of power in the complete PRF can be observed in Fig. 3.7. N_o is obtained by dividing the pixel intensity N by azimuth bandwidth B_a in azimuth profile according to the computation given as follows:

$$N_o = \frac{N}{B_a} = N \times \Delta t. \tag{3.2.5}$$

Note that, pixel intensity is equivalent to noise power for unit resistance.
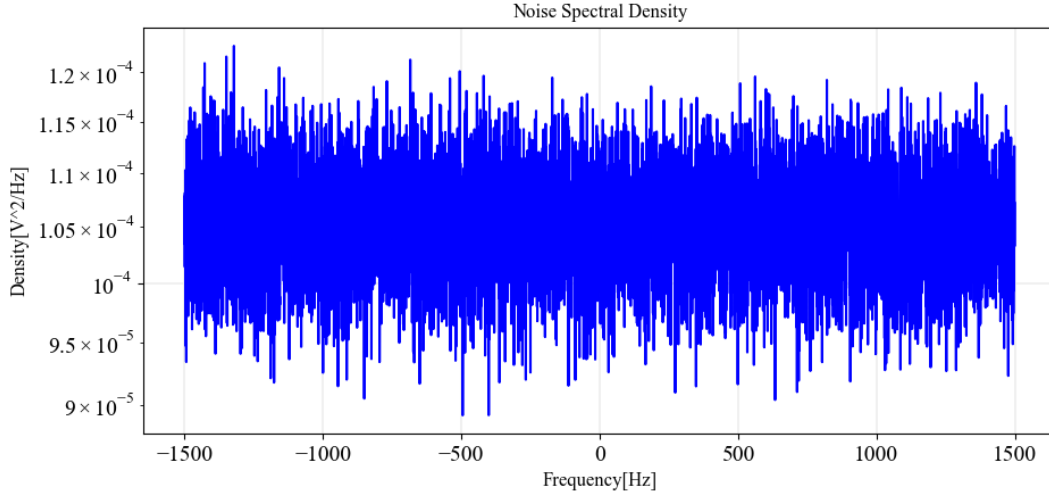
Fig. 3.7: Noise spectral density of SAR image signal $s(t)$.

The comparison of analytically expected values and measured values of the signal intensity, energy, and power spectral density is given in Tab. 3.2.

	Expected	Measured
Intensity $[V^2]$	0.316	0.316
Energy per pixel $[V^2.s]$	1.05×10^{-4}	1.05×10^{-4}
Power Spectral Density $[V^2/Hz]$	1.05×10^{-4}	1.05×10^{-4}

Tab. 3.2: Comparison of measured and expected results.

3.3 Interferogram Statistics

Complex SAR image follows a circular Gaussian process model. This section will present the analytical descriptions of interferogram properties and the influence of coherence on interferometric phase.

The joint PDF of the two complex images i_1 and i_2 is given as [17]:

$$PDF(v) = \frac{1}{\pi^2 |C|} e^{-v^{*T} C^{-1} v}, \tag{3.3.1}$$

where,

$$v = \begin{pmatrix} i_1 \\ i_2 \end{pmatrix} \tag{3.3.2}$$

The covariance matrix can be written as [17]:

$$C = E\left[vv^{*T}\right] = \begin{pmatrix} I_1 & I\gamma \\ I\gamma^* & I_2 \end{pmatrix} \tag{3.3.3}$$

where,

$$I = \sqrt{E\left[|i_1|^2\right] E\left[|i_2|^2\right]}. \tag{3.3.4}$$

and I_1 and I_2 are the expected intensity values of the two images according to equation 3.2.1.

3.3.1 Coherence

Coherence is an important parameter that dictates the phase statistics of the interferogram. Since the images of the same scene are used in interferometry, the quality of the interferogram is determined by the coherence of the two images. The images with low coherence cannot be used in interferometry. In this section, the mathematical descriptions are based on evaluations in [17]. The figure of merit of the interferogram is the complex coefficient defined as [17]:

$$\gamma = \frac{E\left[i_1 i_2^*\right]}{\sqrt{E\left[|i_1|^2\right] E\left[|i_2|^2\right]}}. \tag{3.3.5}$$

Coherence takes value between 0 and 1 such that $0 < |\gamma| < 1$. A decorrelation of $|\gamma|$ is the phase noise determinant, and a $|\gamma| = 1$ suggests that the two images under consideration are identical [17]. The marginal interferometric phase PDF is derived from the joint PDF of interferogram magnitude and phase to give the following relation [17]:

$$PDF(\varphi) = \frac{1 - |\gamma|^2}{2\pi} \frac{1}{1 - |\gamma|^2 \cos^2(\varphi - \varphi_o)} \times$$
$$\left(1 + \frac{|\gamma| \cos(\varphi - \varphi_o) \arccos(-|\gamma| \cos(\varphi - \varphi_o))}{\sqrt{1 - |\gamma|^2 \cos^2(\varphi - \varphi_o)}}\right). \tag{3.3.6}$$

The joint PDF of the magnitude and phase of the interferogram u can be written as [17]:

$$PDF(|u|, \varphi) = \frac{2|u|}{\pi I^2} \exp\left\{\frac{2|\gamma| |u| \cos(\varphi - \varphi_o)}{I(1 - |\gamma|^2)}\right\} \times$$
$$K_o\left(\frac{2|u|}{I(1 - |\gamma|^2)}\right), \tag{3.3.7}$$

where K_o is the modified Bessel function.
φ_o is the mean phase of the interferogram, and is directly related to topography, and is used to for the construction of a DEM. The interferometric phase ambiguously varies from $[-\pi, \pi)$ about the mean value φ_o. The desired mean phase is given as:

$$E[\varphi] = \varphi_o \tag{3.3.8}$$

The variance of the interferometric phase error is related to coherence as follows [17]:

$$\sigma_\varphi^2 = \frac{\pi^2}{3} - \pi \arcsin(|\gamma|) + \arcsin^2(|\gamma|) - \frac{Li^2(|\gamma|^2)}{2}, \tag{3.3.9}$$

where Li represents Euler's dilogarithm.
The loss in coherence can be associated to decorrelation due to several factors [32] such that:

$$\gamma_{total} = \gamma_{SNR}\gamma_{quant}\gamma_{amb}\gamma_{geo}\gamma_{az}\gamma_{vol}\gamma_{temp}\gamma_{proc}, \tag{3.3.10}$$

Where γ_{quant} is due to quantization noise, γ_{amb} is due to ambiguities, γ_{geo} is due to baseline decorreation, γ_{az} is Doppler decorrelation, γ_{vol} is due to volume decorrelation, γ_{temp} is due to temporal decorrelation and γ_{proc} is due to coregistration and processing. The contributions from these decorrelators lead to increase in phase noise. A higher coherence is absolutely necessary for lower phase noise.

Thermal noise is a major contributor of phase noise in the system. In our simulations, only thermal noise will be considered as a major source of decorrelation. The coherence loss due to thermal noise can be stated as [17]:

$$\gamma_{SNR} = \frac{1}{\sqrt{\left(1 + SNR_1^{-1}\right)\left(1 + SNR_2^{-1}\right)}}. \tag{3.3.11}$$

The mathematical descriptions of phase and coherence will be validated with numerical simulations in the next section.

3.4 Generation of SAR Image Pair: Simulations

In this section, two methods to generate complex Gaussian interferometric SAR image pair with varying degree of coherence have been presented. The idea is to compare analytically anticipated statistical results to the measured outcomes from the simulations. The following discussion validates the relation of coherence to the distribution of interferometric phase errors that later will be the basis for the interferometric phase error investigations.

3.4.1 Method 1

The 2D complex SAR image pair $i_1(f)$, $i_2(f)$ with parameters given in section 3.2.1, are generated in the frequency domain with 512 and 8192 samples of the backscattered signal both in range r and azimuth a. Three statistically independent images *Noise A*, *Noise B*, and *Noise C* from circular Gaussian processes are used to produce two such images whose coherence can be varied according to the algorithm described below. The images have mean $\mu = 0$ and unit standard deviation σ in the real and imaginary parts. The simulations have been performed in python. All three images a have afixed number of samples in azimuth but the samples in range can be changed to shift the coherence according to the relation:

$$r_{ovl} = r \times \gamma, \tag{3.4.1}$$

where r_{ovl} is the number of overlapping samples in range, r is the number of samples in range and a is the sample number in azimuth in the image and γ is the coherence coefficient. The number of non-overlapping samples in the image can be given by:

$$r_{non-ovl} = r(1 - \gamma), \tag{3.4.2}$$

The methodology according to 3.4.1 and 3.4.2 for the generation of two SAR images (circular Gaussian) is shown in the block diagram in Fig. 3.8. The simulated 2D complex Gaussian images i_1 and i_2 are shown in Fig. 3.9. After the simulation of two images, the next step is to obtain an interferogram according to equation 2.6.1. The interferogram is obtained from the samples
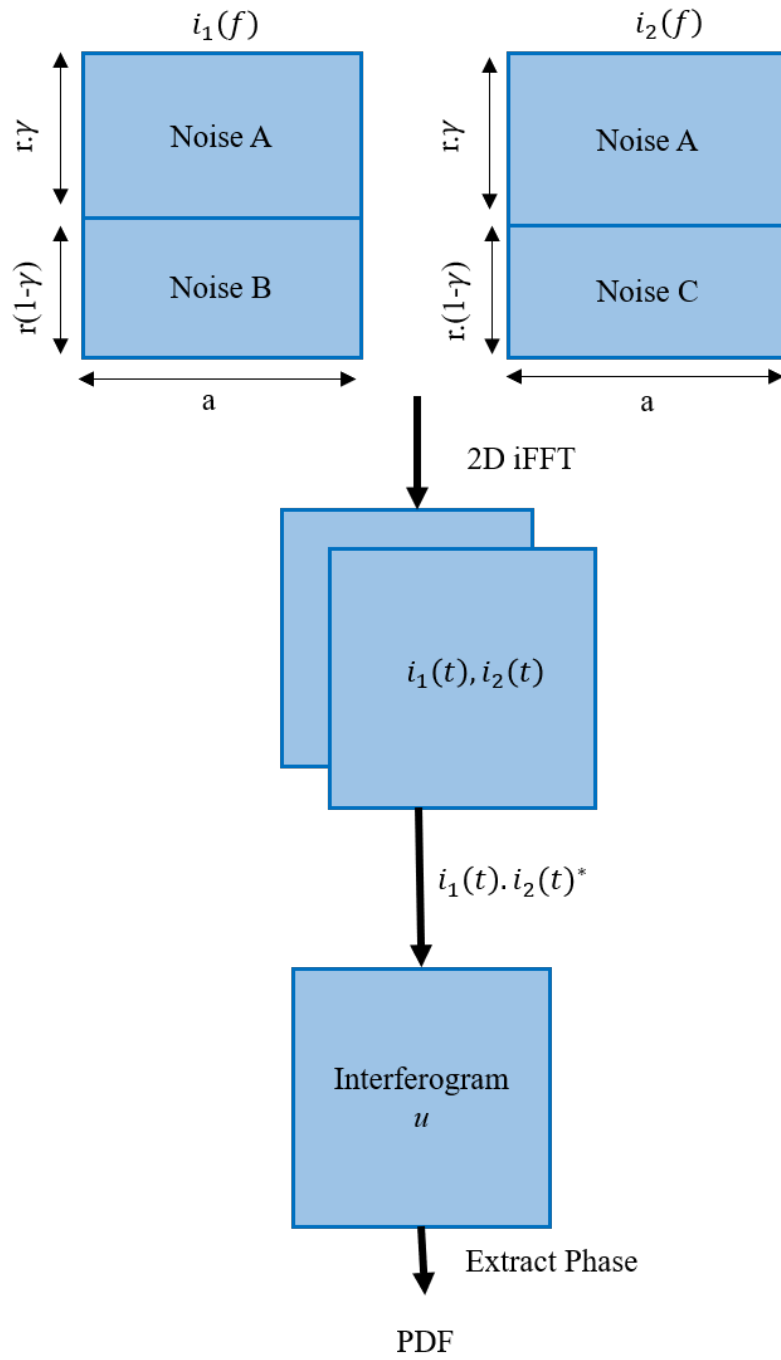
Fig. 3.8: Method 1 of generating complex circular Gaussian interferometric SAR image pair with variable coherence.
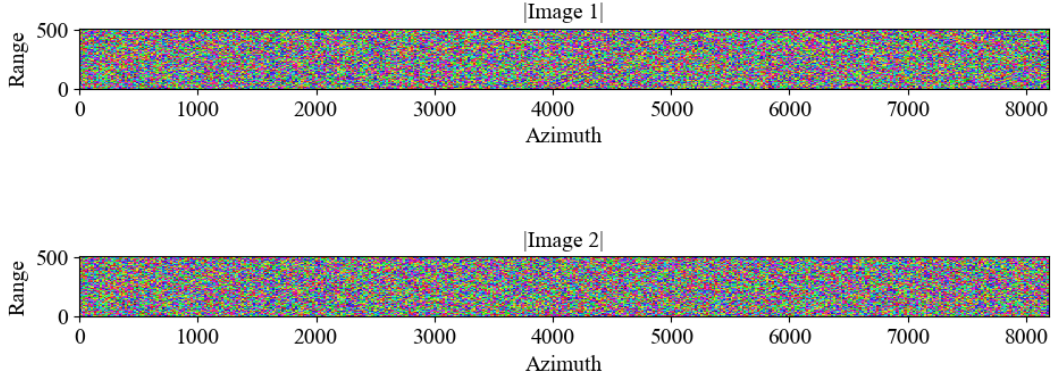
Fig. 3.9: Magnitude of simulated 2D complex SAR images i_1 and i_2.

in time. For that purpose, we take 2D inverse Fourier transform of the samples in range and azimuth.

In the interferogram, it is only the phase information that is meaningful to us to evaluate phase errors. The interferometric phase is obtained from the simulated interferogram and it is observed that the randomly distributed phase in the interferogram is limited to interval $[-\pi, \pi)$ as depicted in Fig. 3.10. In Fig. 3.11, the probability density function of the interferometric phase for three
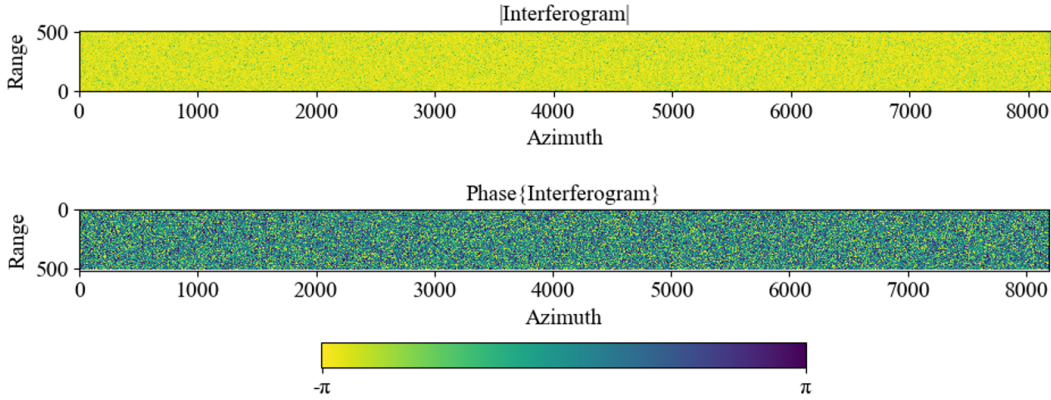
Fig. 3.10: Top: Magnitude of simulated interferogram u. Bottom: Interferometric phase distributed in interval $[-\pi, \pi)$

different values of coherence coefficient $|\gamma|$=0.3, 0.5, and 0.8 is illustrated. It is evident from the plot, that the phase is limited to an interval of $[-\pi, \pi)$. As the correlation between the pixels of the two images reduces, we get more standard deviation in the phase and phase noise increases. For $|\gamma| = 0$, the phase follows uniform distribution indicating that the two images are not correlated and thus the phase difference reveals no useful information.
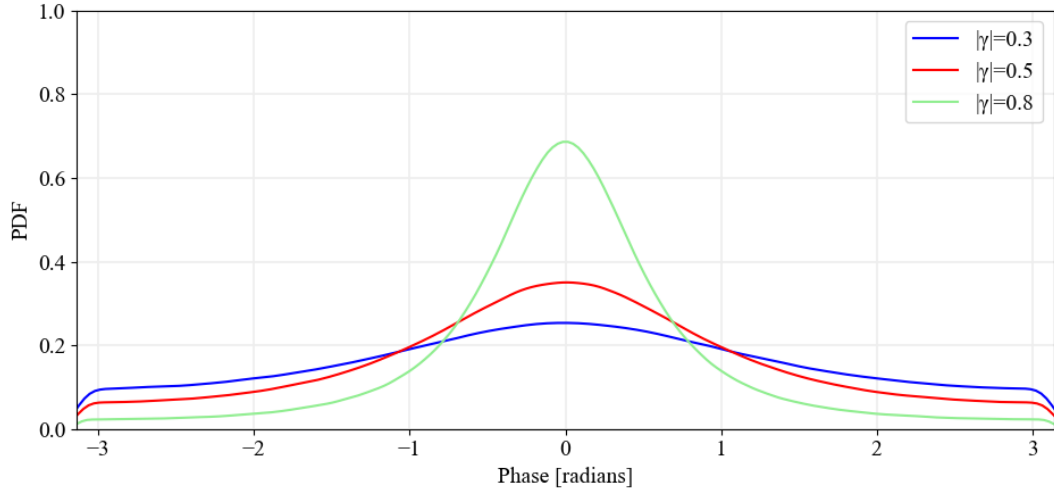
Fig. 3.11: Interferometric phase probability density function for different values of coherence using method 1.

The results of phase standard deviation σ for different values of coherence obtained from analytically derived error predictions using equation 3.3.9 are compared to the errors resulting from the simulations in Tab. 3.3. It can be seen that the phase variance is decreasing with an increase in coherence, and the distribution concentrates towards the mean value and would reduce to a δ function when $|\gamma|$ becomes unity implicating the absence of noise [17].

	$|\gamma|$**=0.3**	$|\gamma|$**=0.5**	$|\gamma|$**=0.8**
Expected σ [radians]	1.542	1.3361	0.9173
Measured value σ [radians]	1.542	1.3363	0.9171

Tab. 3.3: Comparison of expected and measured standard deviation for different coherence values using method 1.

3.4.2 Method 2

The underlying idea of this method is to generate a SAR image pair for the purpose of phase error shift estimation in interferometry and radargrammetry as discussed in [33].

Let us consider three 2D uncorrelated complex circular Gaussian *Noise A*, *B*, and *C* with 512, and 8192 pixel samples backscattered in azimuth a and range r acquired in time domain. The three statistically independent images are combined to yield two SAR images with adjustable coherence. The three images have zero mean and unit variance in the real and imaginary parts. The two SAR images can be expressed as:

$$i_1(t) = \sqrt{(1-\gamma)}A + \sqrt{\gamma}C \tag{3.4.3}$$

$$i_2(t) = \sqrt{(1-\gamma)}B + \sqrt{\gamma}C \tag{3.4.4}$$

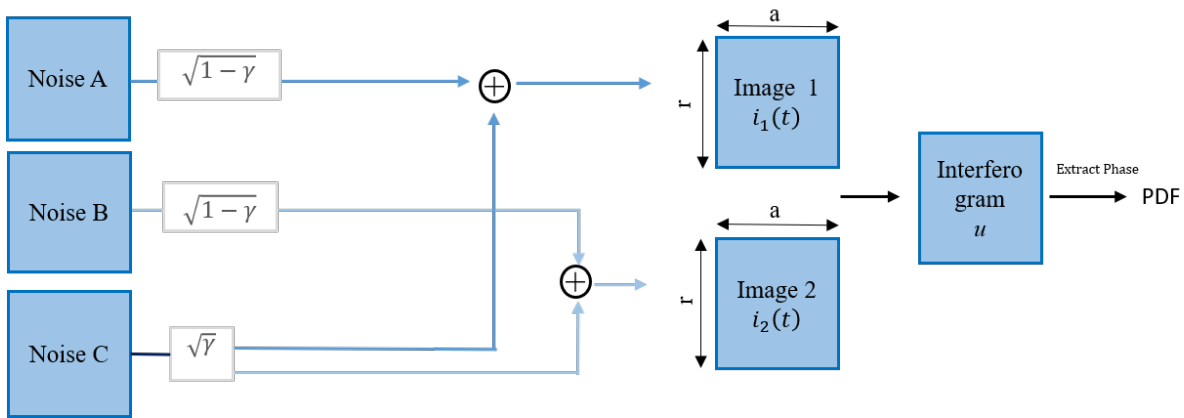The methodology of image generation is depicted in Fig. 3.12. After the image generation, the

Fig. 3.12: Method 2 of generating complex Gaussian SAR images with variable coherence.

next step is to obtain an interferogram. An interferogram of the images i_1 and i_2 is produced using equation 2.6.1 and has a similar pictorial representation as shown in Fig. 3.10 and 3.9. The PDF of this interferogram gives us the estimate of the predicted phase errors that should be consistent with the results that were obtained in *Method* 1. The PDF of the interferometric phase for different coherence values is shown in Fig. 3.13. As expected, phase noise variance
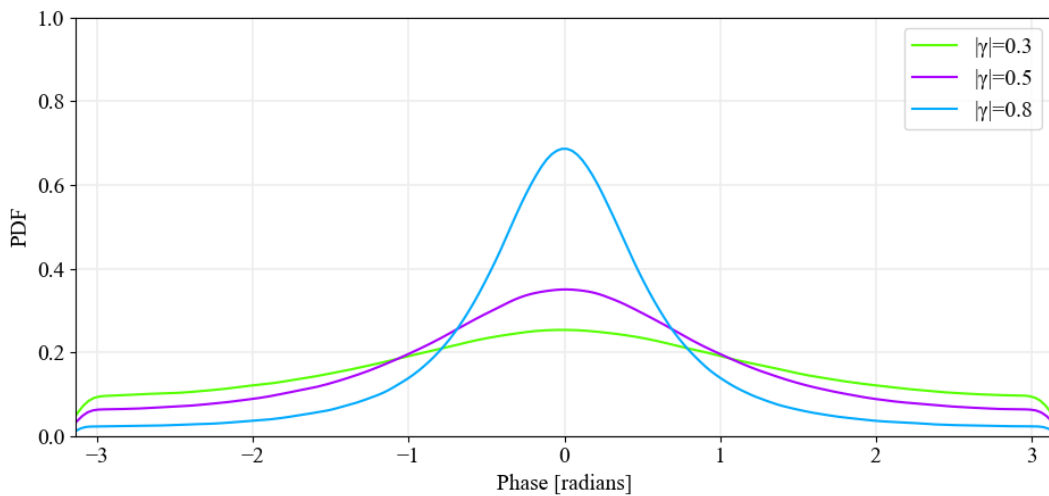
Fig. 3.13: Interferometric phase probability density function for different values of coherence using method 2.

decreases with increasing coherence and the phase values become more consistent and focused around the expected value which is 0 in our case. The analytical phase error predictions are compared to the measurements procured from the simulations in Tab. 3.4.

Therefore, it is concluded that the generation of complex circular Gaussian images using *Method* 1 is equivalent to *Method* 2, and yields same phase error standard deviations for the same values of coherence. In this chapter, the phase statistics of the SAR image pair were studied which gave a detailed demonstration, both analytical and practically implemented of how the phase errors are influenced by the coherence coefficient.

In the next chapter, the image processing and interferometric processing of the SAR image will

	$|\gamma|\mathbf{=0.3}$	$|\gamma|\mathbf{=0.5}$	$|\gamma|\mathbf{=0.8}$
Expected σ [radians]	1.542	1.3361	0.9173
Measured value σ [radians]	1.544	1.3361	0.917

Tab. 3.4: Comparison of expected and measured standard deviation for different coherence values using method 2.

be discussed taking into account antenna pattern and the effect of noise from external sources. The processing will be done for a single look image to derive interferometric phase statistics which will later be analyzed by different averaging techniques to reduce phase noise errors.

4 InSAR Image processing

In the last two chapters, a brief description of SAR interferometry and the goals of our thesis were discussed by providing a detailed understanding of an interferogram, interferometric phase and the ways of establishing relations between the cross-correlation function (coherence) and phase statistics were also mentioned. In this chapter, the methodology of image and interferometric processing of a SAR image will be discussed while considering the antenna pattern during acquisition, its influence on the image spectrum, external noise, power compensation, and side lobe suppression. Complete implementation will be demonstrated by simulation for a single-look complex interferometric SAR image pair and will be extended to multilooking techniques in the later chapters to compare the phase error reduction by different averaging methods in spectral and spatial distribution. This thesis considers multilook and interferometric processing in azimuth dimensions. In the future work, the results can be complimented also for the range dimension. The azimuth dimension is considered more challenging as the antenna pattern has an effect on the azimuth spectrum and azimuth look generation. During acquisition from distributed scatterers, the samples in range and azimuth corresponding to the same scene can be in different resolution cells. Therefore, a modification is needed to shift the pixel in the right resolution cell by the cross-correlation of the images. This is called coregistration. After shifting, the complex conjugate of the coregistered image (slave) is finally multiplied with the second (master) image to form an interferogram. In our simulations, we will consider that the pixels are already coregistered and are arranged in the right resolution cell.

4.1 Single look SAR performance

The following simulations have been performed in python with the aim of generating a backscattered signal giving two identical image signals from a homogeneous scene with inherent coherence 1 and an interferometric phase of $0°$, which provides later directly the PDF of phase errors. The White Gaussian noises are added along with certain SNRs to the images which are usually considered due to the receiver noise and other factors that alter the coherence of a signal. Then after the addition of noise to the signal, we will have two images that contain the same information deteriorated by some noise and essentially represent a SAR image pair. Different cases such as, first: signal processing without antenna pattern weighting, second: signal processing with antenna pattern weighting will be studied to understand the influence of antenna pattern on the SAR image.

The image signal processing will be performed in consideration with the parameters given in Tab. 4.1. The block diagram in Fig. 4.1 describes the methodology of the image signal processing. A complex Gaussian random signal $s(t)$ is generated in the time domain with PRF as the sampling rate in azimuth and Fs is the sampling rate in range. These parameters have been used for the performance simulations throughout. In InSAR, identical images of a scene are acquired. But due to varying parameters such as look angle, their coherence changes during acquisition. The phase of the signal is randomly distributed in an interval of $[-\pi, \pi)$. The spectra of the raw complex image signals are depicted in Fig. 4.2. The signals have constant power distributed for
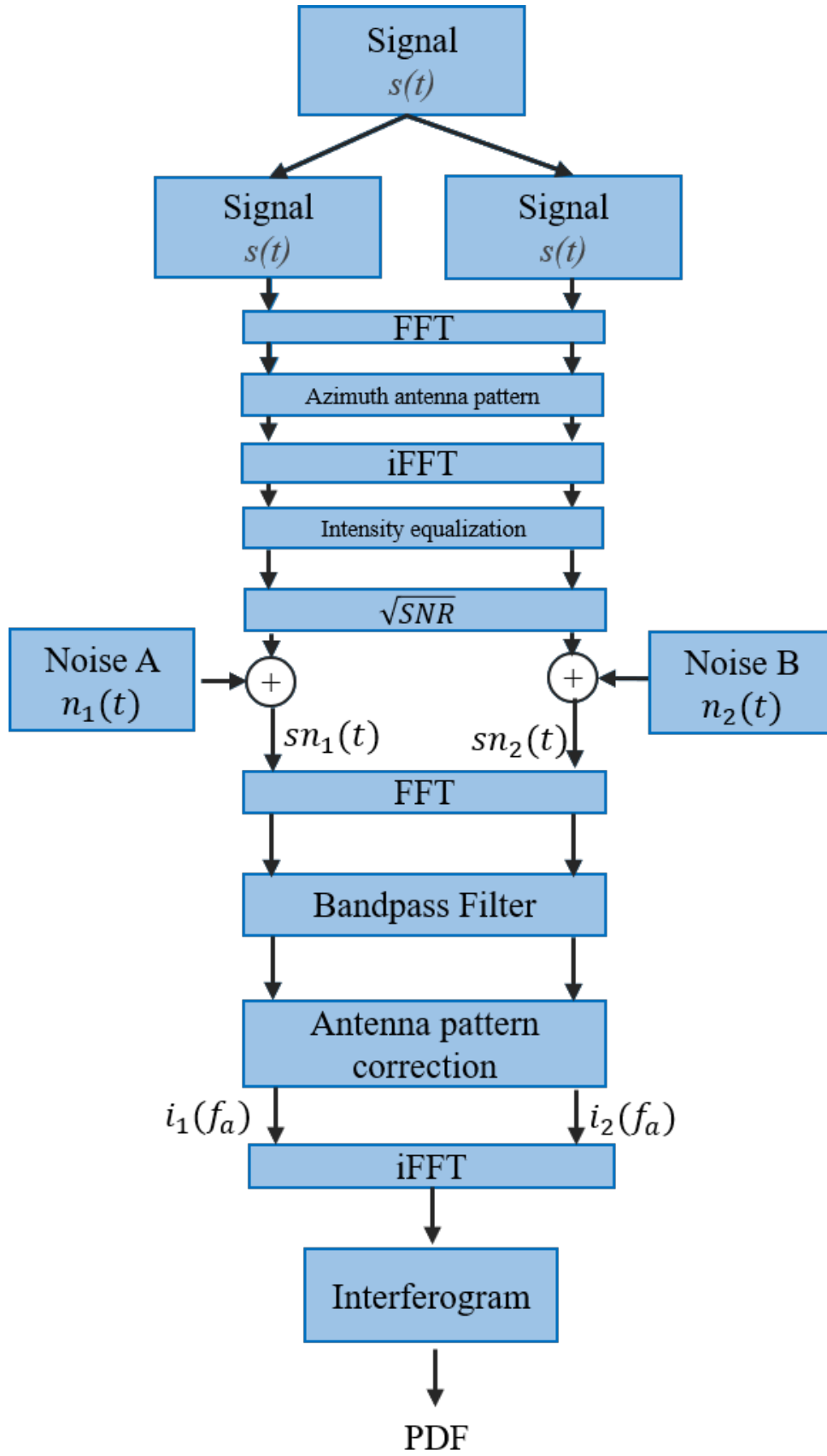
Fig. 4.1: Methodology of SAR image signal processing simulation.

Parameter	Value
Samples in range and azimuth	512, 8192
PRF	3000 Hz
Azimuth acquisition bandwidth	3000 Hz
Fs	100 MHz
3 dB processed Bandwidth B_a	2782 Hz
Azimuth sampling interval	0.3 ms
Range sampling interval	5.12 μs
Signal and Noise power (N)	25 dBm = 0.316 V^2
Standard deviation σ	0.397
Mean μ	0
SNR in two images	10 dB

Tab. 4.1: Parameters of complex Gaussian SAR image pair.

all azimuth frequencies. The pixel intensity of the signal is given by:

$$I_p = |s(t)|^2 = 0.316 \, \text{V}^2. \tag{4.1.1}$$
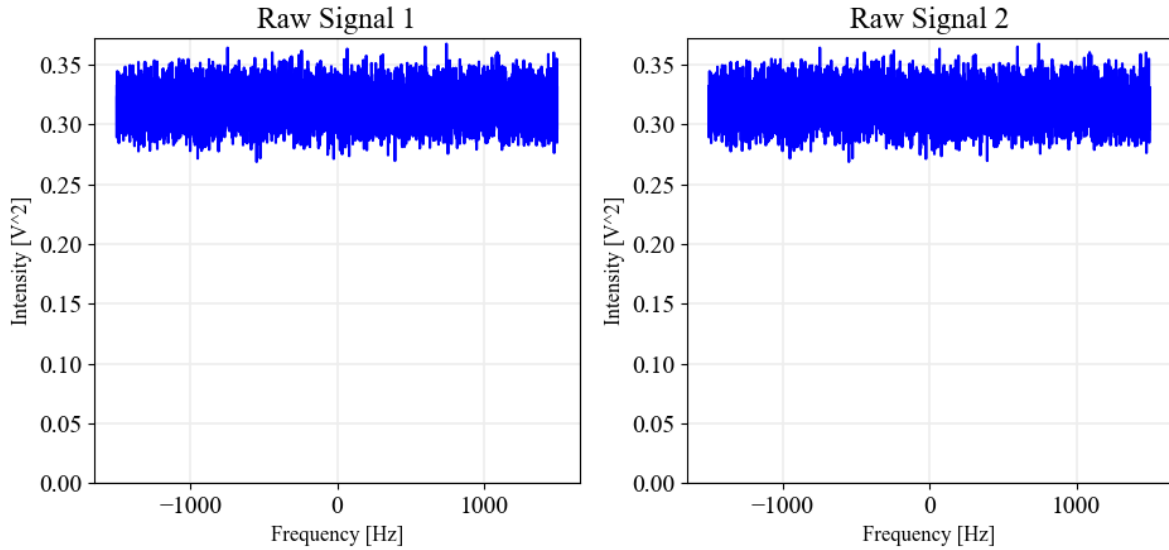
Fig. 4.2: Raw complex SAR signals.

4.1.1 Case 1: No Antenna Pattern

In this section, the raw signals are processed without taking into account the antenna pattern. The acquired signals are modeled to have an SNR of 10 dB. The main source of noise is thermal noise and thus it is considered as a dominant source and is modeled by Additive White Gaussian Noise (AWGN). The image processed bandwidth is considered to be equivalent to the azimuth acquisition bandwidth as no antenna pattern is present. The results will be compared with the

other cases in later sections. It should be noted that, antenna pattern is a characteristic of acquisition and cannot be avoided. We can only choose to compensate for the antenna pattern weighting during signal processing.

4.1.2 Case 2: Antenna pattern

During acquisition, the signal is influenced by a two-way antenna pattern of the radar. Simulations were performed to analyze the impact of an approximated antenna pattern in azimuth on a SAR image. The image signals have echoes in azimuth and range in the spatial domain. The image is transformed to the spectral domain by applying Fast Fourier Transform (FFT) in azimuth to get frequency distribution. The one-way antenna amplitude pattern as a function of azimuth angle is numerically simulated using a *sinc* function according to the relation:

$$A(\theta) = \text{si}(\frac{0.885}{0.33}\sin(\theta)). \tag{4.1.2}$$

To map the radiation pattern in frequency domain, the antenna pattern as a function of azimuth angle θ is transformed to a function of azimuth frequency according to the following relation:

$$f_a = \frac{2V_s}{\lambda} \times \sin(\theta), \tag{4.1.3}$$

Interpolation is carried out to convert non-uniform distribution into uniform frequency distribution. In equation 4.1.3, the azimuth frequencies f_a corresponding to the azimuth angle θ are evaluated. V_s is the satellite velocity which is set to $7600 \, \text{m/s}$ and $\lambda = 0.03 \, \text{m}$ is the X-band wavelength. The two-way $6 \, \text{dB}$ beamwidth of $0.33°$ corresponds to $2782 \, \text{Hz}$ processing bandwidth of the antenna B_a. Fig. 4.3 (a) shows the two-way antenna pattern which is typically a sinc squared pulse as a function of azimuth angle and, (b) shows the two-way antenna pattern as a function of azimuth frequency. The radiation pattern amplitude is marked with a blue line and 6dB beamwidth level is marked with a red line. The antenna pattern in processed bandwidth B_a is applied to the signal only in the azimuth direction and the spectral weighting due to it causes reduction in intensity as certain frequencies are suppressed by the antenna pattern and thus deteriorating the quality of the pixels in the image. The spectrum of the signal before and after the antenna pattern weighting is shown in Fig 4.4. The complex signal $s(f)$ is influenced by the antenna pattern such that:

$$S(f_a) = s(f) \times |A(f_a)| \tag{4.1.4}$$

where $|A(f_a)|$ is the two-way amplitude pattern of the antenna. Note that, for convenience, here we assumed an unrealistic antenna pattern that has no gain outside the 6 dB two-way region. This can be done later as well in the processing, by applying a bandpass filter in azimuth that limits the processed bandwidth to this 6 dB area. As the signal amplitude gets altered by the antenna pattern, the intensity of the frequency samples in the spectrum is changed and is not uniform anymore. To evaluate the signal intensity after the antenna pattern, the signal is transformed to the spatial domain. The reduction in the signal power has to be compensated to maintain pixel intensity by an amplitude equalization factor x given as follows:

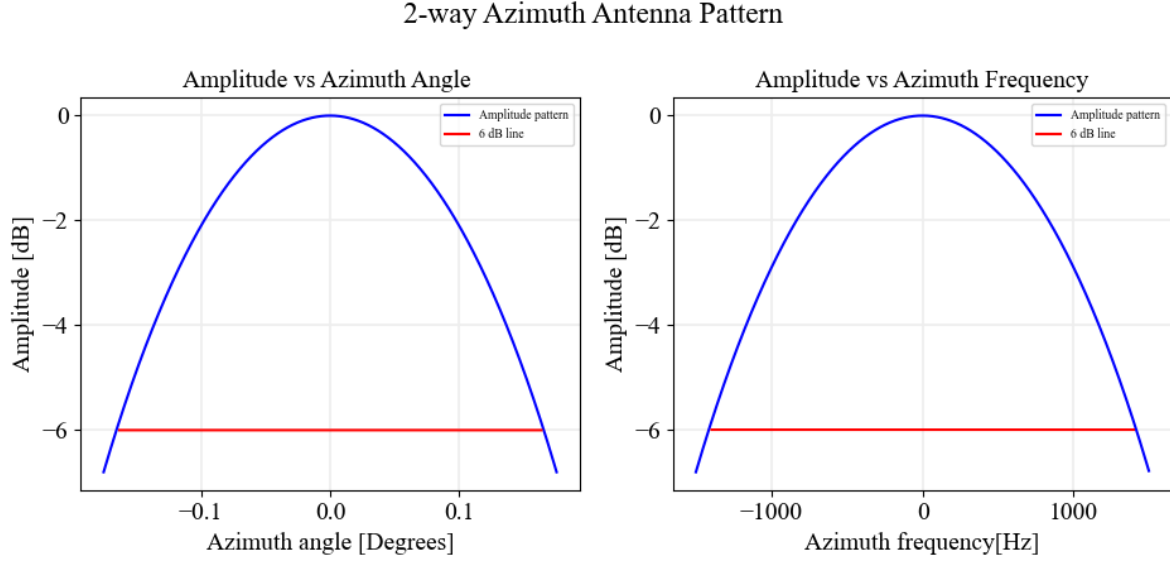$$x = \sqrt{\frac{\int_{PRF} 1.df_a}{\int_{B_a} P_a(f_a).df_a}}, \tag{4.1.5}$$

Fig. 4.3: (a) Two-way antenna pattern against azimuth angle, (b) Two-way antenna pattern against azimuth frequency. The amplitude pattern for entire azimuth bandwidth level is marked with blue color and 6 dB beamwidht is marked with red line.

	Intensity [$\mathbf{V^2}$]
Raw signal	0.3161
Signal after antenna pattern	0.2051
Signal after equalization	0.3161

Tab. 4.2: Signal intensity comparison.

with $P_a(f_a)$ being the azimuth antenna pattern in two-way. The intensity of the signal is equalized such that:

$$s(t) = s(t_a) \times x. \tag{4.1.6}$$

The constant normalized spectrum integrated over the entire acquisition bandwidth is divided by the power of the azimuth antenna pattern over the processed bandwidth B_a. The equalization factor x gives us a weighted image spectrum after taking an FFT of the image with the original intensity of the raw signal. The intensities before and after the azimuth antenna pattern and after the equalization are mentioned in Tab 4.2. In a SAR image spectrum, pixels in the outer edges have higher noise compared to the inner regions where the SNR is maximum. So, increasing the signal intensity also implies higher phase noise in the outer region of the spectrum. The processed bandwidth determines the resolution. During azimuth processing, the antenna pattern is equalized and the azimuth modulation originating from the sensor movement relative to the target is removed. After this removal, only the constant phase remains. If we have a constant antenna pattern, we get a narrow beamwidth and better resolution but higher sidelobes. Therefore, weighting is performed for the sidelobe reduction in the azimuth impulse response (IRF) at the expense of resolution. To approximate this sidelobe suppression without increasing the phase noise in the outer spectrum, antenna pattern correction can be performed in combination with a spectral weighting that is in effect an approximation for the azimuth antenna pattern itself [34]. The next step in interferometric processing simulation is the adjustment of the SNR. The same
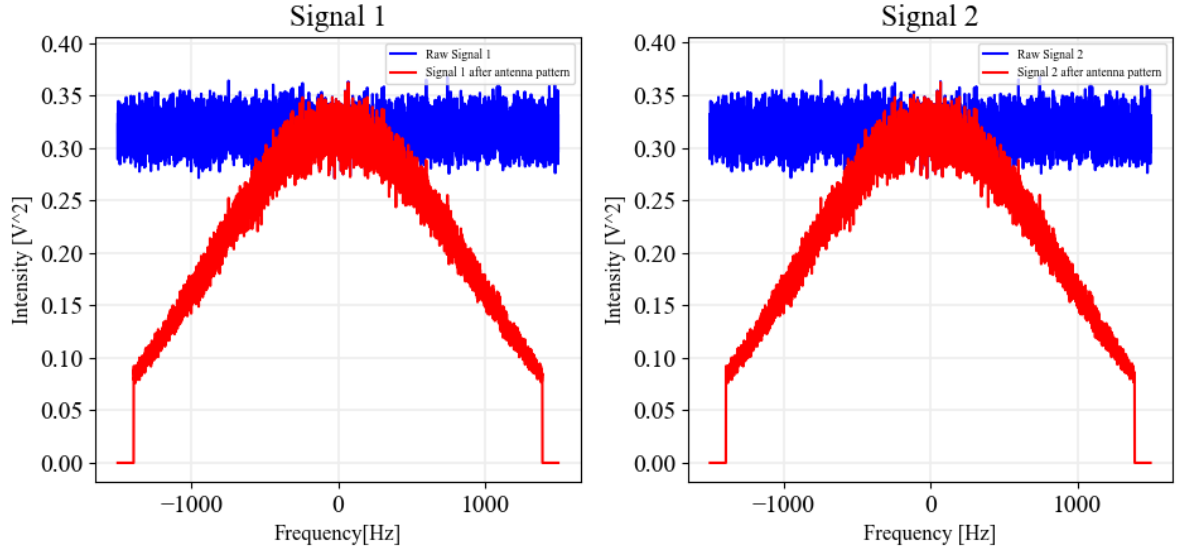
Fig. 4.4: Illustration of complex SAR signal spectra before and after the antenna pattern weighting. Signal marked with blue is the raw complex signal acquired from a scene. Signal marked with red is the signal after the influence of antenna pattern weighting.

SNR of 10 dB is used for both images. Let us assume, the additional noise corresponds to an SNR of 10 dB. SNR is added to the signal according to the following relation [31]:

$$s(t) = s(t) \times \sqrt{SNR}. \tag{4.1.7}$$

This changes the real and imaginary parts of the standard deviation of the signal to [31]:

$$\sigma_{new} = \sigma.\sqrt{SNR} = 0.706 \tag{4.1.8}$$

The noise components due to thermal noise are added to the signals. This noise is modeled by two AWGN signals $n_1(t)$ and $n_2(t)$ and are added to the two complex SAR signals as follows:

$$sn_1(t) = s(t) + n_1(t) \tag{4.1.9}$$

$$sn_2(t) = s(t) + n_2(t) \tag{4.1.10}$$

Note that, same standard deviation was used in the generation of the real and imaginary parts of the signal as well as in the generation of two noises. The SNR of signals $sn_1(t)$ and $sn_2(t)$ can be evaluated by the relation [31]:

$$SNR = \frac{I_{sn_1}}{I_{n_1}} - 1 = \frac{I_{sn_2}}{I_{n_2}} - 1 \tag{4.1.11}$$

The coherence value is also related to the SNR in the two images. Assuming SNR to be the only source of decorrelation, using equations 3.3.11, 4.1.11 and 3.3.5, analytically expected values are compared to the values measured from above simulations in Tab 4.3. As the noise is spread throughout the azimuth bandwidth, it is filtered by a digital bandpass filter filter with passband frequency range $-B_a/2 < f_a < B_a/2$ along with the signal in the processed bandwidth. Now, two cases of azimuth processing will be considered exclusively for antenna pattern correction

and no antenna pattern correction on the image spectra. in SNR in the complex signal. The comparison of SNR[1], coherence $|\gamma|$ and standard deviation of the interferometric phase σ is given in Tab. 4.3.

	SNR dB	$|\gamma|$	σ [radians]
Signal with noise after bandpass filter	10	0.773	0.965
Image signal after antenna pattern correction	9.3	0.745	1.012

Tab. 4.3: Comparison of measured values of SNR and coherence at different stages of processing.

- **Antenna pattern correction:** The antenna pattern correction on the new signal and the noise is performed to compensate for the azimuth weighting applied on the signal according to equation 4.1.4. The complex signals are divided by the amplitude of the two-way antenna pattern such that:

$$i_1(f_a) = \frac{sn_1(t)}{|A(f_a)|}, \tag{4.1.12}$$

$$i_2(f_a) = \frac{sn_2(t)}{|A(f_a)|}, \tag{4.1.13}$$

where $i_1(f_a)$ and $i_2(f_a)$ are the two processed SAR images that will be used to form an interferogram during interferometric processing whose spectra are depicted in Fig 4.5. The images are assumed to be coregistered. From Fig. 4.5, it is clearly observed that after the
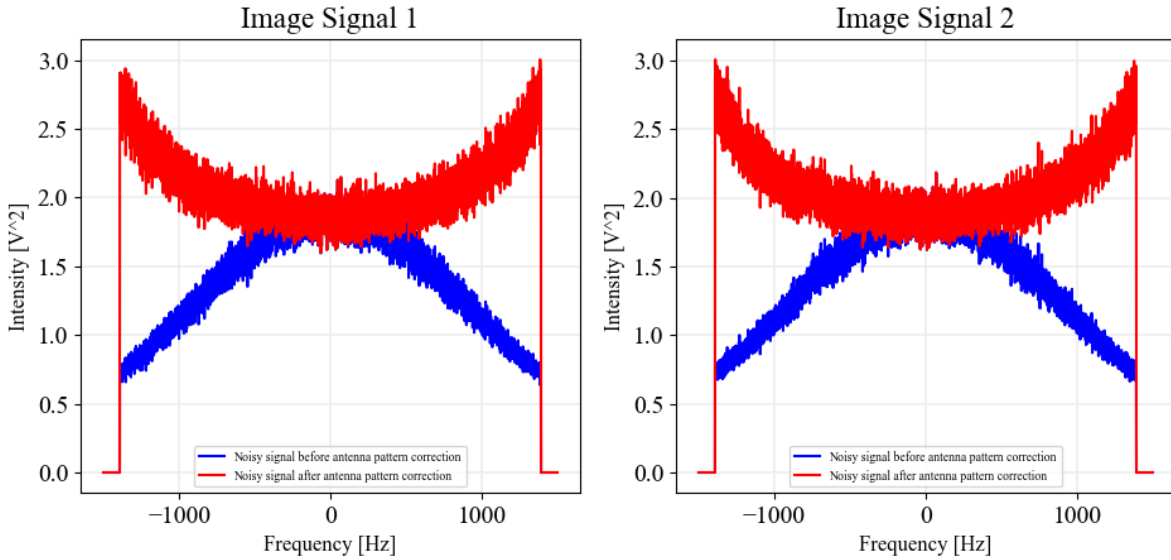
Fig. 4.5: Complex SAR signal spectra before antenna pattern correction represented by blue curve and after antenna pattern correction represented by red curve.

antenna pattern correction, the noise in the outer spectra is substantially increased. The SNR is much better in the center of the spectra where there is maximum illumination. This augmented phase noise contributes to significant increase in phase errors. To analyze

---

[1]Note: There is a variation of ± 0.6 dB due to a different bandwidth of noise than that of the antenna processed bandwidth. However, the variation is small and can be neglected.

the interferometric phase errors, the image pair is transformed to the spatial domain distribution by carrying out an inverse FFT (iFFT), and the interferogram u is formed using equation 2.6.1.

- **No antenna pattern correction:** As seen above, antenna pattern correction causes an increase in phase noise in the outer spectrum of the image. Let us now consider a case where no antenna pattern correction is performed. In this case, complex signals $sn_1(t)$ and $sn_2(t)$ are directly used to compute an interferogram using equation 2.6.1. The image spectra without antenna pattern correction are shown in Fig. 4.6.
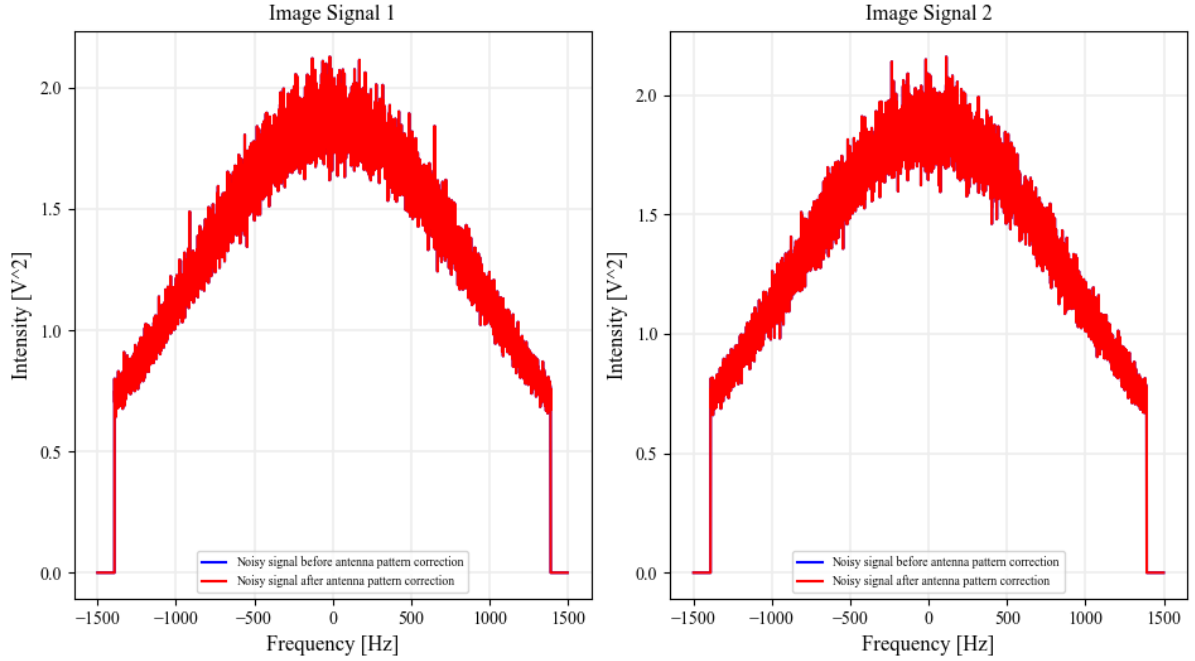
Fig. 4.6: Image signal spectra with no antenna pattern correction.

4.2 Results and Comparison

In single look image processing for **Case 1**, it is observed from the above simulations that the influence of antenna pattern is crucial for the signal as it helps in achieving better coherence as mentioned in Tab. 4.3 but at the cost of reduced resolution. The PDF of interferometric phase for single look performance without the influence of antenna pattern on the signal is given in Fig. 4.7. The standard deviation and coherence are mentioned in Tab. 4.4. Note that, the antenna pattern is inherent to the SAR acquisition. We can only decide to correct for it or not to correct for it.

	Measured	Expected
$\|\gamma\|$	0.76	0.76
σ [radians]	0.988	0.987

Tab. 4.4: Comparison of expected and measured values of standard deviation and coherence for Case 1.
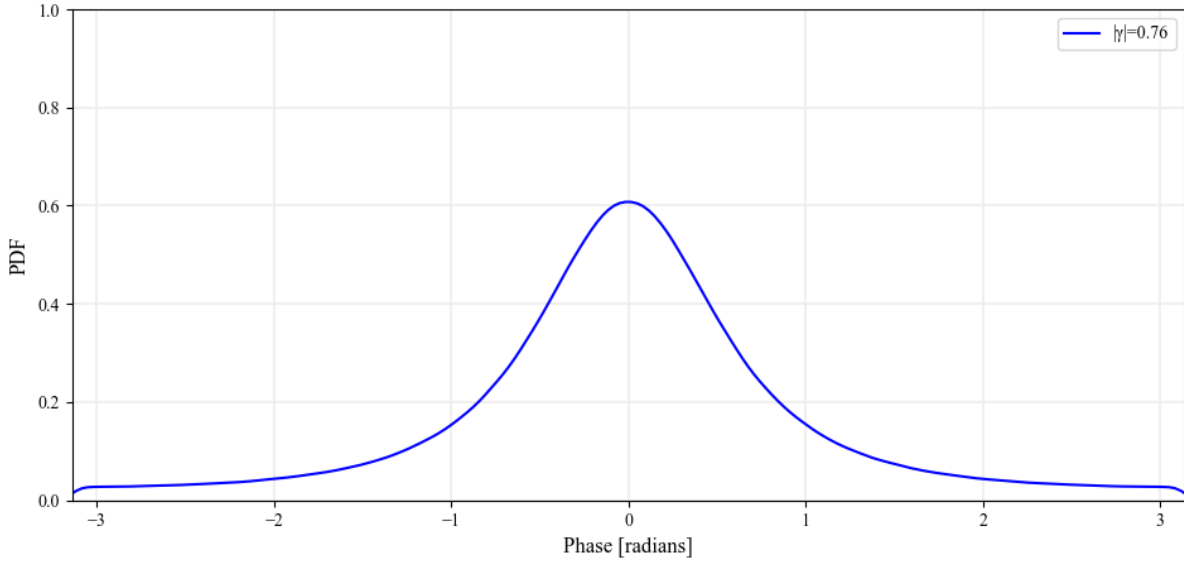
Fig. 4.7: Probability density function of interferometric phase without the influence of antenna pattern correction on the image signal.

For **Case 2**, the influence of antenna pattern with correction leads to a reduced coherence because of the increase phase noise of the pixels in the outer spectrum of the image. This can be avoided by using a suitable window after the antenna pattern instead of performing pattern correction. However, that is out of scope for the work in this thesis. The comparison of standard deviation and coherence with and without antenna pattern correction is given in Tab. 4.5 . The comparison of PDF of interferometric phase for both the cases can be observed in Fig. 4.8. It can be clearly seen that antenna pattern correction leads to deterioration of performance by reducing coherence and increasing standard deviation of interferometric phase. From Tab. 4.5, it

	$|\gamma|$		σ **[radians]**	
	Measured	Expected	Measured	Expected
Without pattern correction	0.77	0.77	0.965	0.965
With pattern correction	0.745	0.745	1.012	1.012

Tab. 4.5: Comparison of expected and measured values of standard deviation and coherence for Case 2.

is evaluated that the antenna pattern correction leads to a reduction of coherence by a factor of 1.03 and an increase in standard deviation by a factor of 0.95.

In this section, the SAR image processing was thoroughly discussed and the error predictions were compared for different scenarious during interferometric processing that lead to variations in interferometric phase errors. The increase in phase noise poses a need for error correction techniques in SAR to improve phase difference measurement accuracy for height estimation for accurate construction of a DEM. In the next chapter, various error correction methods will be investigated and compared.
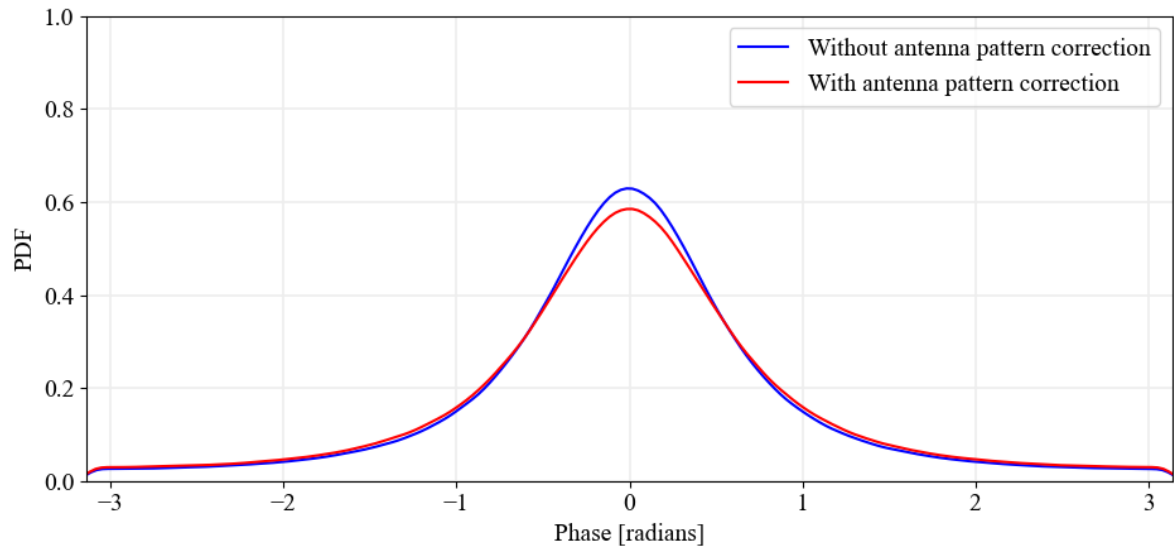
Fig. 4.8: Probability density function of interferometric phase. PDF for image spectra without antenna pattern correction is marked in blue, PDF for image spectra with antenna pattern correction is marked in red.

5 Phase Error Reduction Methods

The contribution of phase noise makes it challenging to unwrap phase errors to get the absolute phase. Extensive research has been performed to deduce techniques for phase noise reduction by several techniques such as spatial averaging and multilooking [35]. In the previous chapters, the characterization of phase errors was done. In this chapter, the focus will be on the discussion of existing methods of phase error reduction.

The first approach will be the spectral averaging of low-resolution SAR image called multilooking. The performance of the error reduction depends on the number of looks. The comparisons will be presented for several degrees of multilooking. The second approach will be to apply sliding spatial averaging on the interferogram itself to get rid of small-time variations and coarseness. The results will be compared for measured results. The demonstrated error correction methods will be validated using simulated interferograms in the following sections. The shortcomings of averaging methods will be presented. Finally, a new parameter for statistical evaluation of these averaging methods will be proposed that is based on test scenario with increasing toggling frequency between two phase values.

5.1 Multilooking

Multilooking is a well-established image enhancement technique in SAR image processing. It is essentially used for mitigation of speckle noise. In multilooking, the synthetic radar aperture is divided into shorter apertures that produce low resolution SAR images of the same scene in the azimuth dimension, which is considered in this thesis. The total bandwidth of the SAR images that have been processed in azimuth is divided into smaller bandwidths to obtain multiple narrow bands also known as *looks* [17]. These look images are then used to compute low resolution independent interferograms corresponding to each band. These interferograms are then coherently added resulting in reduction of the phase noise. The multilook performance is dependent on the number of looks. Let us assume that we want to evaluate the phase from K looks which is typically K number of interferograms u[n]. The phase contributions from terrain are assumed to be consistent in all the interferograms. According to the maximum likelihood estimator (MLE) [17]:

$$\varphi'_{MLE} = arg \left\{ \sum_{n=1}^{K} u[n] \right\} \tag{5.1.1}$$

The PDF of the multilook phase estimation characterized by number of looks can be expressed as [17]:

$$PDF(\varphi', K) = \frac{\Gamma(K + \frac{1}{2})(1 - |\gamma|^2)^K |\gamma| \cos(\varphi - \varphi_o)}{2\sqrt{\pi}\Gamma(K)(1 - |\gamma|^2 \cos^2(\varphi - \varphi_o))^{K+\frac{1}{2}}} + \frac{(1 - |\gamma|^2)^K}{2\pi} {}_2F_1(K, 1; \frac{1}{2}; |\gamma|^2 \cos^2(\varphi - \varphi_o))$$

(5.1.2)

The PDF is obtained considering that looks in the data are independent. For the estimation of statistical performance of dependent looks, [36] proposes a model to obtain effective number of looks which is essentially less than the conventional number of looks.

Intuitively, the phase deviations are likely to occur from pixel samples with small amplitude as the noise has strong impact on them and can easily deviate the phase. The pixels with higher amplitudes have phase close to the mean value as the effect of noise on them is lower. Therefore, the averaging of the interferograms leads to a reduction of phase noise by a factor of $\frac{1}{\sqrt{K}}$ [17].

In continuation of image processing, where a processed image is obtained after the antenna pattern correction, the image spectrum is divided into multiple looks before computing the interferogram as depicted in Fig. 5.1. Let us divide the spectrum of each individual SAR image
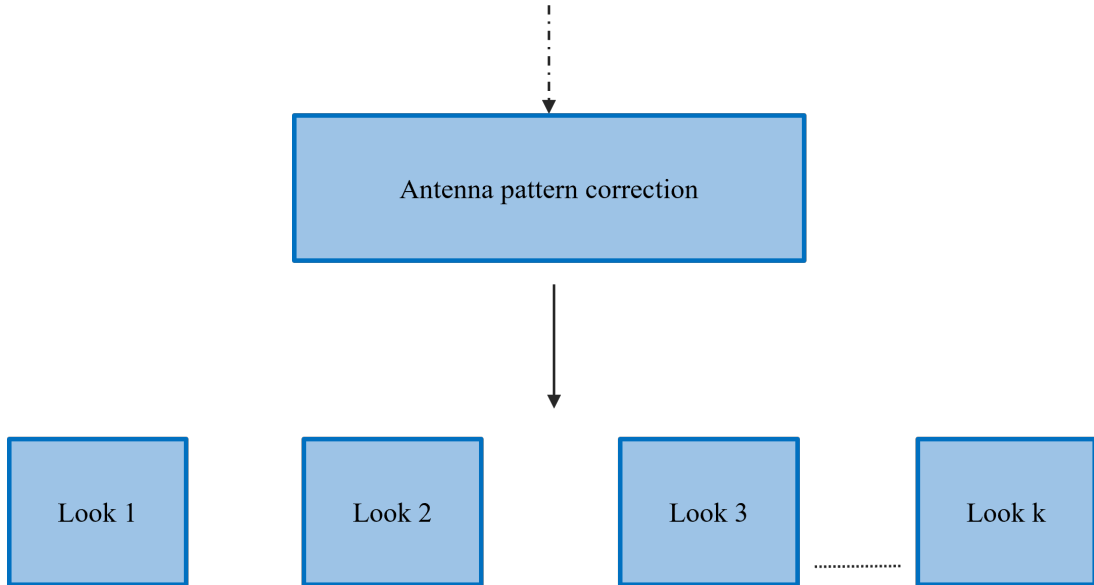
Fig. 5.1: Multilooking

of the interferometric image pair into $K = 8$ looks. In this case, 8 independent interferograms are computed for each look from the two images $i_1(f_a)$ and $i_2(f_a)$. The complete azimuth processing spectra of the image pair is divided into 8 sub-spectra each such that the bandwidth of each look is 347.75 Hz. The looks are generated by interpolation of the samples outside the bandwidth of sub-spectrum so that there is no aliasing in the respective looks. The looks in the complex SAR image pair are only employed in azimuth, and a single look is maintained in the range. In the following sections, multilooking will be implemented on the image spectrum with antenna pattern correction and without antenna pattern correction.
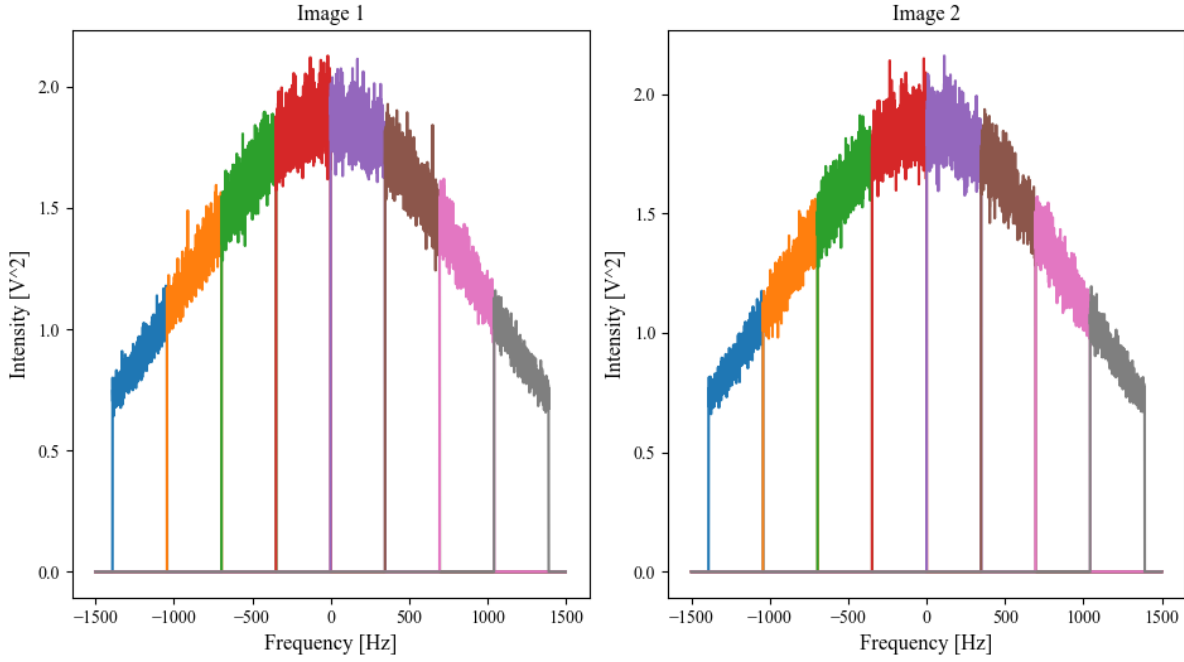
Fig. 5.2: SAR image spectra without antenna pattern correction divided into 8 looks without antenna pattern correction.

5.1.1 Without Antenna Pattern Correction

Without performing antenna pattern correction on the image, the spectrum is divided into 8 looks with 347.75 Hz as bandwidth of each look. The SAR image pair spectra can be observed in Fig. 5.2.

The SNR of each look[1] in the two image spectra evaluated according to equation 4.1.11 is mentioned in Tab. 5.1. From the above table, it is evidently clear that the looks on the outer

Look (k)	SNR [dB]	
	Image 1	Image 2
1	5.11	5.11
2	9.42	9.42
3	12.24	12.20
4	13.61	13.6
5	13.60	13.58
6	12.23	12.25
7	9.45	9.48
8	5.16	5.16

Tab. 5.1: SNR in SAR image 1 and 2 with no antenna pattern correction.

edges of the spectrum have poor SNR and inner looks of the spectram have considerably higher SNR and therefore the phase noise is least in the inner spectra with maximum illumination of the pixel implying high intensity and lower phase noise. The overall SNR in the complete spectra

---

[1]Note: k is the independent look index and K is the total number of looks the spectrum is divided into.

Look (k)	$\|\gamma\|$	$\sigma_{measured}$ [radians]	$\sigma_{expected}$ [radians]
1	0.64	1.16	1.16
2	0.74	1	1.02
3	0.80	0.91	0.91
4	0.82	0.86	0.87
5	0.82	0.86	0.87
6	0.80	0.91	0.91
7	0.74	1	1.02
8	0.64	1.16	1.16

Tab. 5.2: Coherence and standard deviation in interferometric phase for 8 looks with no antenna pattern correction.

of the two images is 10 dB respectively.

The expected coherence $|\gamma|$ is estimated for each independent look using equation 3.3.11 that relates coherence with the SNR in the images and the interferometric phase standard deviation σ of each look is estimated using the numerical simulations and analytically using equation 3.3.9. The discussed parameters are mentioned in Tab. 5.2. Although, it has been observed that this coherence estimate for large number of looks tends to overestimate the coherence and becomes asymptotically biased by the influence of systematic errors as discussed in [17]. To obtain unbiased coherence from the estimated coherence, Cramér Rao bound can be used [17]:

$$var(|\gamma|)_{CR} = \frac{(1 - |\gamma|^2)^2}{2K}. \tag{5.1.3}$$

[37] discusses several estimators to compute asymptotically unbiased coherence.

The probability density function of the interferometric phase after implementing 8 looks on the image spectrum can be seen in Fig. 5.3. It can be seen that the interferometric phase is concentrated around the mean phase 0. By performing comprehensive simulations, the standard deviation σ in interferometric phase is obtained for single look performance and various degrees of multilooking as given in Tab. 5.3

Looks (K)	σ [radians]
1	0.965
2	0.642
4	0.381
8	0.229
16	0.152
32	0.104

Tab. 5.3: Interferometric phase standard deviation for different number of looks without antenna pattern correction.
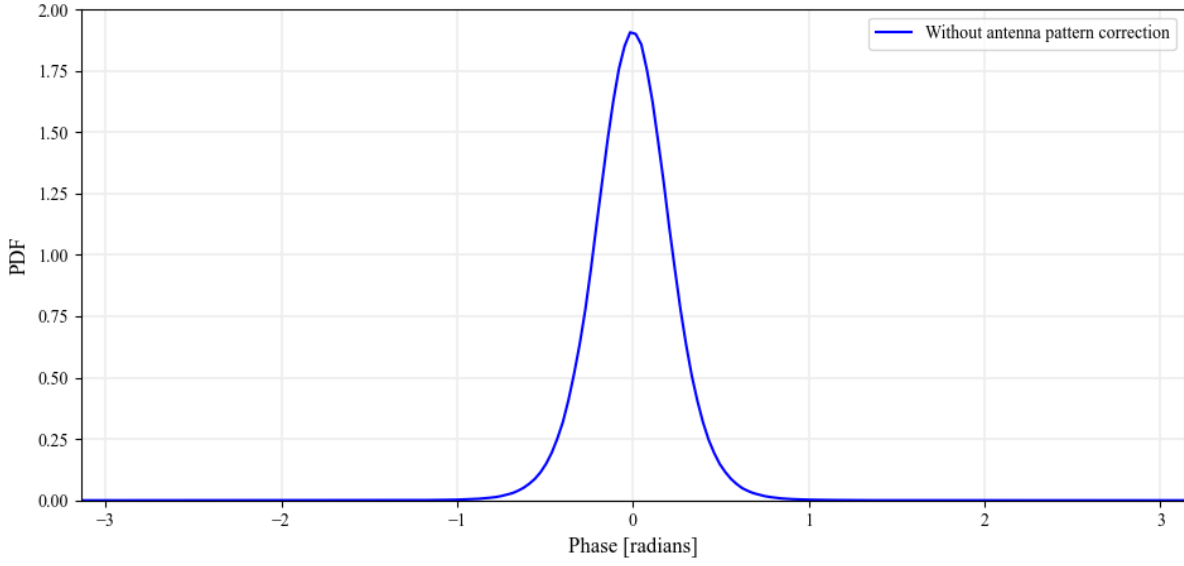
Fig. 5.3: Probability density function of interferometric phase for 8 looks without antenna pattern correction.

5.1.2 With Antenna Pattern Correction

The spectra of the complex SAR image pair are divided into $K = 8$ looks in a similar manner as discussed above. The bandwidth of each independent looks spectrum is 347.75 Hz. The SNR of the indepdendent looks in the image spectrum calculated using 4.1.11 are stated in Tab. 5.4. Tab. 5.4 and 5.1 give a comparison of the SNR in the individual looks of the interferometric SAR image pair for cases involving antenna pattern correction and without antenna pattern correction. And it can be observed that the outer look have lower SNR in case of antenna pattern correction. From the divided spectrum in Fig. 5.4, it can be observed that the looks in the outer spectra have increased phase noise due to the antenna pattern correction. Therefore, the outer looks have more interferometric phase standard deviation. The useful SAR signal backscattered from the ground is weighted by the antenna pattern. The thermal noise that rises in the Low Noise Amplifier after the antenna is not useful. Therefore, a correction of the antenna pattern for the useful signal, i.e the constant amplitude of the spectrum rises up the noise component in the signal.

Look (k)	SNR [dB]	
	Image 1	Image 2
1	4.8	4.8
2	9.3	9.3
3	12.17	12.17
4	13.58	13.55
5	13.57	13.55
6	12.17	12.14
7	9.36	9.33
8	4.86	4.86

Tab. 5.4: SNR in SAR image 1 and 2 with antenna pattern correction.
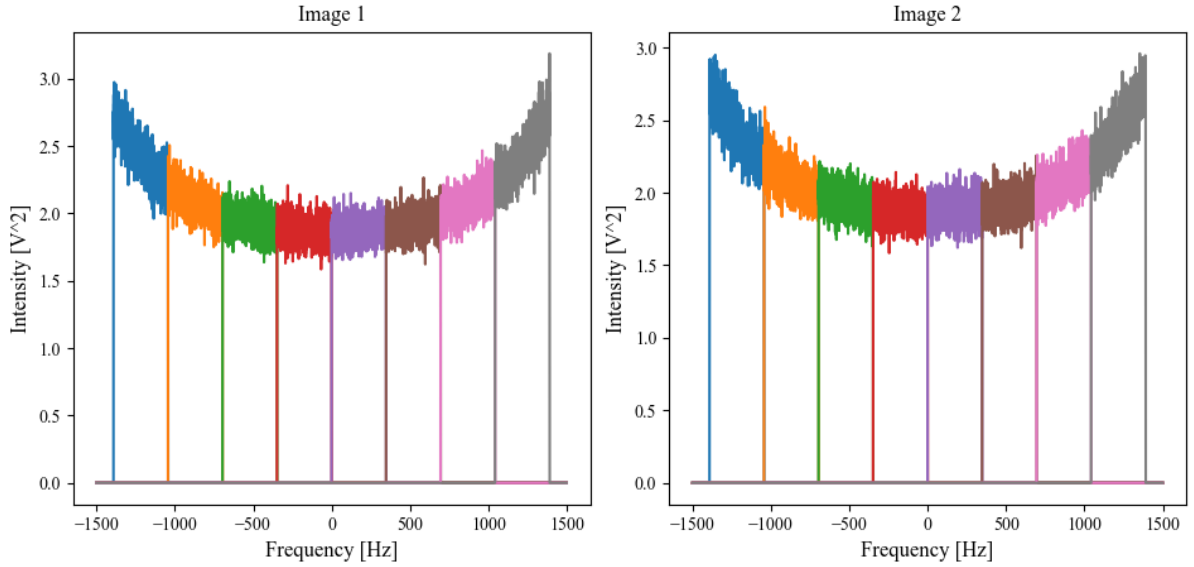
Fig. 5.4: SAR image spectra with antenna pattern correction divided into 8 looks.

The total intensity of the signal can be seen in Fig. 5.4. The coherence $|\gamma|$ and interferometric phase standard deviation σ are given in Tab. 5.5. The comparison of the probability density

Look (k)	$|\gamma|$	$\sigma_{measured}$ [radians]	$\sigma_{expected}$ [radians]
1	0.63	1.17	1.16
2	0.74	1.01	1.02
3	0.80	0.91	0.91
4	0.82	0.86	0.87
5	0.82	0.86	0.87
6	0.80	0.91	0.91
7	0.74	1	1.02
8	0.64	1.16	1.16

Tab. 5.5: Coherence and standard deviation for 8 looks for the case with antenna pattern correction.

function of the interferometric phase for the case with and without antenna patter correction is shown in Fig 5.5 while performing multilooking with 8 looks. As expected, the phase concentrates around the mean phase 0 and standard deviation is reduced significantly as compared to the single look case, but yields more standard deviation and reduced coherence as compared to 8 look processing of without antenna pattern correction case. The interferometric phase standard deviation for various degrees of multilooking is mentioned is Tab. 5.6 w.r.t the single look case. It can be seen from the table that the standard deviation is higher for every look as compared to the standard deviation for the case where no antenna pattern correction was made. This is due to the increased phase noise in case of antenna pattern correction as discussed earlier.

Based on simulations, multilooking has proven to be a good solution that allows for pixel by pixel noise reduction by reducing the bandwidth by spectral averaging [38]. However, the phase noise is reduced at the expense of geometric resolution. As the number of looks are increased,

Looks (K)	σ [radians]
1	1.01
2	0.694
4	0.42
8	0.254
16	0.168
32	0.116

Tab. 5.6: Standard deviation for different number of looks for the case with antenna pattern correction.
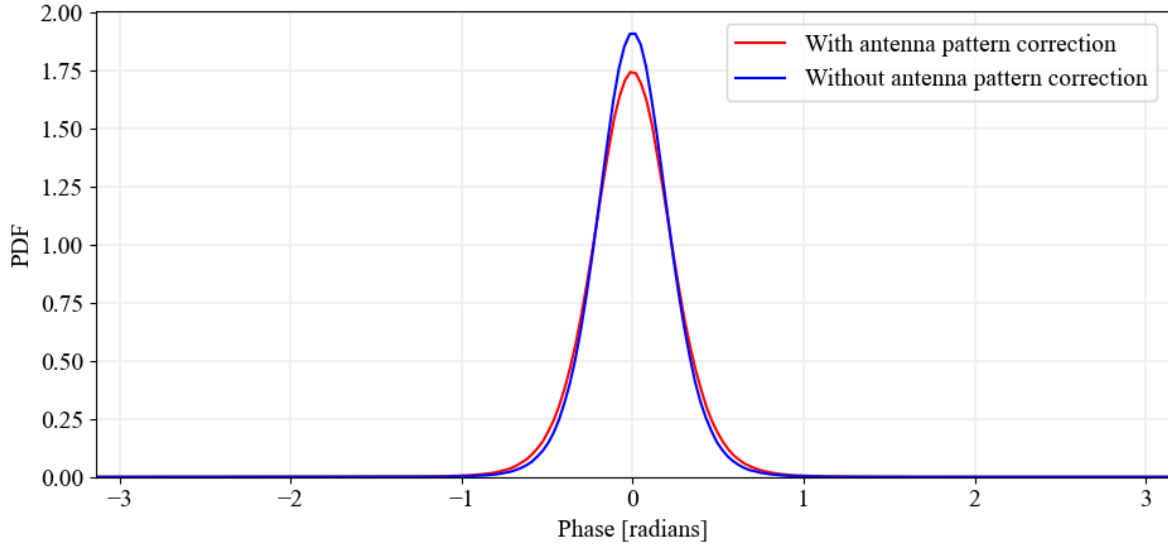
Fig. 5.5: Probability density function of interferometric phase. Blue curve depicts for the case without antenna pattern correction, and red depicts for the case with antenna pattern correction for multilooking with 8 looks.

the geometric resolution decreases. Therefore, a trade-off between the resolution and phase noise should be found. Additionally, in case of antenna pattern correction, use of several weighting windows can provide to be an optimal solution for sidelobe suppression. In that case, overlapping looks can be used while performing multilooking to better exploit the phase spectrum [39]. It is not preferable to perform multilooking on the SAR image spectra if no antenna pattern correction is performed because for the non-uniform amplitude due to the antenna pattern weighting, the SAR impulse response function for each look is not uniform. Therefore, in that case, moving average can be performed on the interferogram as described in the following sections.

5.2 Spatial Averaging by Moving Average

The complex SAR data has phase fluctuations that contribute to phase noise. These phase jumps can be reduced by averaging the pixels arranged in time by a sliding window that reduces the irregularities that appear in the phase. It can also be understood as a technique to smoothen the pixel properties to diminish phase jumps. Boxcar Filter which is analogous to moving average by

a rectangular window is typically a low pass filtering process that removes the high frequency components from the data. It is one of the most widely used local statistical image filters that is implemented for denoising of pixels in the images [40]. Being a local filter, it is important that it can only be applied to coregistered images as it only works when the pixels in the neighborhood belong to the same scattering scene. In this method, while carrying out the moving average, the intensity of a pixel is set in accordance with the averaged intensities of its neighboring pixels. And thus, all pixels are close to the expected value therefore down-scaling the variations and diminishing the noise. The number of averaged samples depends on the size of the window. However, there is a limit to length the window size that can be used as averaging the pixel intensity also results in loss of details which makes edge detection difficult.

It is important to note that for the phase noise reduction, the moving average is applied on the complex interferogram i.e. the real and imaginary parts undergo same moving average operation. This is equivalent to addition of complex pointers. Also, it is worth mentioning that moving average can principally be executed both in range and azimuth dimensions. In this thesis, we focus on moving average on the complex interferogram only in the azimuth dimension.

In the following simulations, different window lengths performance will be assessed by estimation of coherence values and corresponding standard deviations. A boxcar filter can be defined as [40]:

$$Box(P_i) = \frac{1}{W_i} \sum_{j \epsilon W_i} P_j \tag{5.2.1}$$

Where P_i is the pixel under consideration in the interferogram and W_i is the set of pixels in the sliding window.

A moving average filter is smoothing filter that acts as a rectangular window in time domain. The spectrum of the interferogram is weighted by a wide si function with relatively high sidelobes. Therefore, we apply two moving averages in sequence, which in effect acts as a moving average with a triangle function. In the interferogram, this lowers the sidelobes of the si weighting. And so, to perform sidelobe suppression on the spectrum of interferogram, variants of moving average filters with different windows or cascaded filters can be used. Doing the moving repeatedly results in different kinds of windows that can be chosen depending on the required sidelobe suppression of the samples in stopband in frequency domain. The moving average window shape is be demonstrated in Fig. 5.6. Here, n is the window size of a rectangular window and $2n$ is the window size of a triangular window that results from convolution of the two cascaded rectangular windows.

5.2.1 Without Antenna Pattern Correction

The moving average is applied on the interferogram considering no antenna pattern correction was performed on the image spectra. The averaging is done such that the intensity of the pixel under consideration is set to an average value of its neighboring pixels within the window, simultaneously causing a reduction in the phase errors. The moving average has been implemented on every azimuth line in the interferogram and the corresponding phase standard deviations σ have been recorded in Tab. 5.7 for different window sizes[2]. It should be noted that these window sizes correspond to the two rectangular windows. For example, a rectangular window of size 2 is applied twice to achieve a standard deviation of 0.642.

---

[2]n is the window size of one rectangular window. 2n is the resultant size of the triangular window.
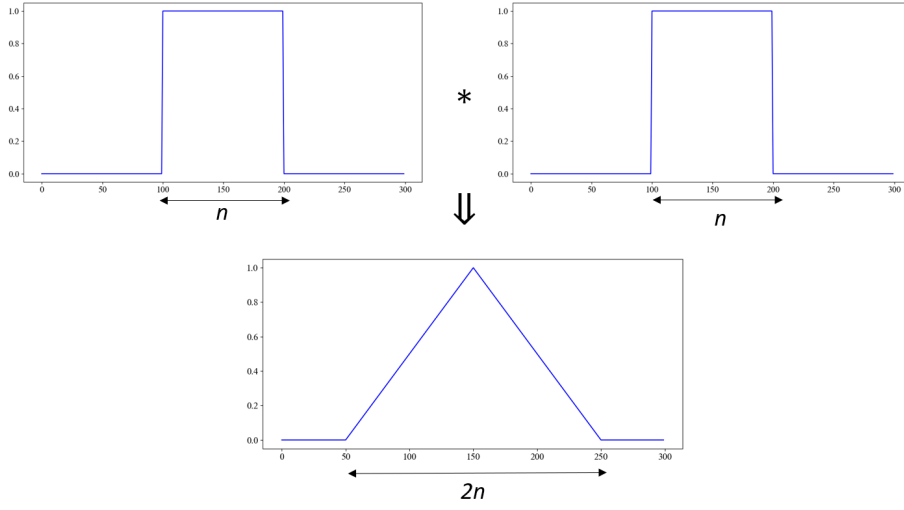
Fig. 5.6: Two cascaded rectangular windows of length n result in a triangular window of length 2n.

Window size (n)	σ [radians]
1	0.965
2	0.642
4	0.389
8	0.2311
16	0.156
32	0.111

Tab. 5.7: Interferometric phase standard deviation for different moving average window sizes without antenna pattern correction.

5.2.2 With Antenna Pattern Correction

In this case, the moving average is applied on each azimuth line of the interferogram that has been obtained with the complex image spectra after performing antenna pattern correction on them. The phase standard deviations σ with different window sizes (2) are mentioned in Tab. 5.8. The results from the above simulations conclude that the error reduction performance of the repeated boxcar filter improves with the increasing size of the window. The standard deviation reduces significantly with increasing window size as can be seen from Tab. 5.8. However, using this kind of local filter also leads to resolution degradation and is only applicable for homogeneous scenes with Gaussian scatterers.

Window size (n)	σ [radians]
1	1.01
2	0.691
4	0.421
8	0.236
16	0.157
32	0.108

Tab. 5.8: Interferometric phase standard deviation for different moving average window sizes with antenna pattern correction.

5.3 Proposed Parameter for Comparison of Phase Error Reduction Methods: MFPC

In our simulations until now, a constant phase with mean $\mu = 0$ was considered. This corresponds to a constant height to be measured and allows for measuring direct interferometric phase error in interferogram. However, in real measurements, the phase of interferogram is not constant and has lot of phase variations that reflect the elevation in scene. After all, this is the quantity to be measured in the interferogram. The radar is sensitive to these phase variations.

For comparison of phase noise reduction methods, multilooking and moving average is done in terms of reduction of interferometric phase errors i.e. reduction in phase error standard deviation. However, the effect on the height details that can be measured needs to be accounted for, too. In SAR image processing, the quantity is the geometric resolution. Multilooking or moving average reduce the speckle but deteriorate the geometric resolution. For interferograms, the standard deviation of the interferometric phase error provides the information about what height differences can be measured. But for interferograms, the geometric resolution does not directly give information about what variation in the interferometric phase can be measured. Therefore, in this section, a new parameter for interferometric performance estimation is proposed called as *Maximum detectable Frequency of Phase Change (MFPC)*, that measures the highest frequency of interferometric phase change that is possible.

A test scene has been used with linearly increasing phase change frequency. For understanding the behavior of this test scene, the fourier analysis provides a good appreciation of the detectable phase change frequencies.

For this purpose, phase modulation is performed on the master SAR image by modeling a phase scene with linearly increasing phase change frequency. There is a highest phase change frequency that is detectable in the interferogram after interferometric processing for error reduction, and this highest frequency shall be estimated. The idea of investigation is depicted in Fig. 5.7. The phase change frequency is linearly increasing in azimuth direction and it is shown that for higher phase variations, the MFPC comes down from the maximum frequency present in the phase scene after averaging. PRF is the maximum detectable frequency of phase change in a scene. Frequencies higher than the PRF will undergo undersampling and cannot be detected at all. The phase scene modulation is done according to the following relation:

$$s_{Master}(t) = s(t) \times \exp(j\phi_a), \tag{5.3.1}$$

where $s(t)$ is the raw SAR image signal, $s_{Master}(t)$ is the Master SAR image acquired during interferometric acquisition, and ϕ_a is the test phase scene. The test phase scene is obtained using
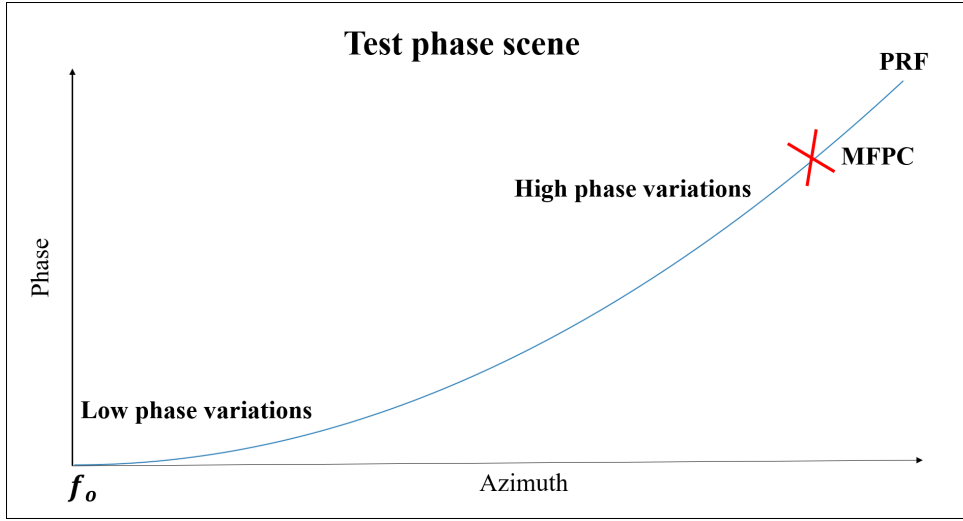
Fig. 5.7: Phase test scene with linearly increasing frequency of phase change in azimuth direction.

a complex frequency sweep signal such that [41]:

$$x(t) = \cos(2\pi f(t)t) + j\sin(2\pi f(t)t), \tag{5.3.2}$$

where $f(t)$ is the linearly varying frequency function given by [41]:

$$f(t) = \frac{kt}{2} + f_o, \tag{5.3.3}$$

where, k is the rate of change of frequency. With linearly varying frequency, signal phase takes a quadratic form as [41]:

$$\phi_a = 2\pi \left(\frac{k}{2}t + f_{start} \right) t + \phi_o, \tag{5.3.4}$$

where ϕ_o is the initial phase of the signal which is set to 0 in the following. The frequency modulated phase of the signal $x(t)$ is applied to the raw complex master SAR signal in azimuth according to equation 5.3.1. The rate of change of frequency in the test phase scene k is obtained as:

$$k = \frac{f_{end} - f_{start}}{T}, \tag{5.3.5}$$

where $f_{start} = 0\,\text{Hz}$ and $f_{end} = 700\,\text{Hz}$ are the starting and ending frequencies respectively at duration $T = 2.73\,\text{seconds}$. The real part of the frequeny modulated signal $x(t)$ sampled at $PRF = 3000\,\text{Hz}$ is shown in Fig. 5.8 (a). Fig. 5.8 (b) and 5.8 (c) depict phase and phase map of the test scene respectively. The investigations of the test phase scene influence for MFPC are performed for the cases involving antenna pattern correction and without antenna pattern correction on the signal spectra where the same phase variation in azimuth has been applied to all range lines. In practical, the phase error reduction methods performed on the interferogram or on the image pair spectra tend to average out the phase errors. During simulations, it was also observed that along with the phase errors, the reduction in the resolvable frequency of the phase change is also reduced as a result of spatial and spectral averaging. The numerical simulations are done for both error reduction methods i.e Multilooking and Spatial averaging by moving average with a cascaded rectangular window as discussed earlier in this chapter. The

interferometric phase affected by the phase scene can be observed in Fig. 5.10. The SNR of the SAR image pair is maintained as $10\,\mathrm{dB}$ throughout the simulations as no antenna pattern correction is performed. The two cases involving with antenna pattern correction and without antenna pattern correction have been investigated because in practice, both approaches are applied depending on the emphasis on resolution during image processing or interferometric phase errors during interferometric processing.
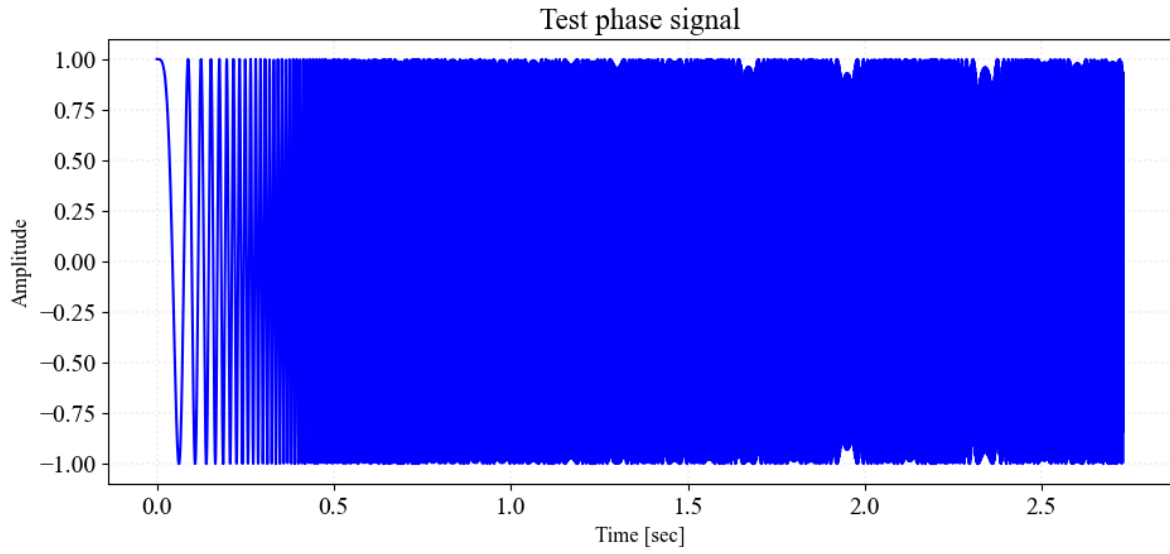
(a) Real part of the amplitude of the frequency modulated test phase scene signal $x(t)$.
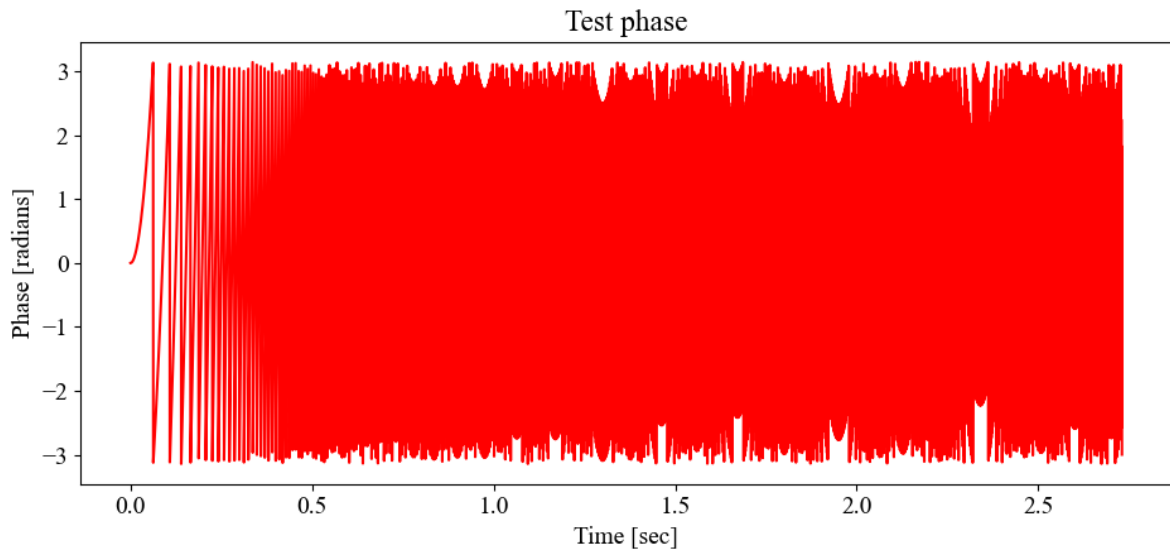
(b) Phase of the test scene.

51
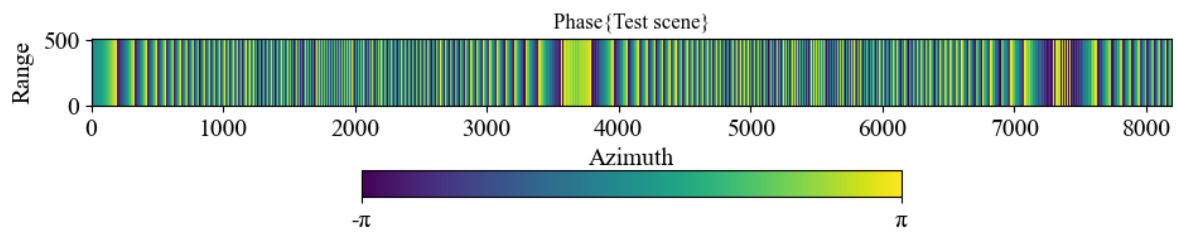
(c) Phase map of the test scene.

Fig. 5.8: Test phase scene with linearly increasing frequency of phase change.

- **Case 1: Without antenna pattern correction:** During interferometric processing of the SAR image pair, no antenna pattern correction has been performed on the complex image spectra. Similar to modulation transfer function (MTF) in optics, a Spectrum of Interferometric Phase (SIP) is obtained by taking FFT in azimuth of the interferometric phase. The spectrum of the interferometric phase after averaging is obtained by taking FFT of the phase from one azimuth line of the interferogram and for better visualization, the profile of the FFT of all the azimuth lines is generated. The azimuth profile of the FFT of phase in all azimuth lines is obtained by averaging the phase in all range lines. The modification in Fig. 2.5 including the phase scene combined for cases with and without antenna pattern correction is shown in Fig. 5.9. The red blocks represent the modifications involving test phase scene. The phase spectrum obtained is depicted in Fig. 5.11.

  From the SIP in Fig. 5.11, the maximum observable frequency is verified as 700 Hz which is the maximum frequency in the generated test phase scene. The amplitude of this phase change frequency is obtained by taking 50% decay value in the SIP amplitude. This amplitude corresponds to 0.0055. Similarly, 50% decay in amplitude has been used to calculate the cut-off detectable frequency of the spectra for different averaging method cases.

  Let us analyze the performance behavior of the test phase scene in azimuth profile if multilooking is performed on the interferometric SAR image spectra during image processing with different number of looks. The interferometric phase map of the multilooked analysis with 8 looks is depicted in Fig. 5.13. From the figure it can be observed that only lower frequencies of phase changes are visible. The higher frequencies are subsided as a result of averaging. Lower frequencies have higher phase amplitude and the phase variation is less and therefore, the effect of noise is not strong enough to cause deviation in their phase. However, for higher frequencies, phase changes rapidly and averages to 0. In the spectrogram in Fig. 5.14, the intensity of higher frequencies can be observed in 1 azimuth line and in azimuth profile after averaging. It becomes clear the in 1 azimuth line in 5.14 (b), the intensity of the phase is high for low frequencies but drops to very low values for higher frequencies. Phase frequency response in azimuth profile in 5.14 (a) represents a better visualization of the phase behavior. For further cases, only SIP in azimuth profile is shown. From Fig. 5.12, it can be seen that on performing multilooking on the complex image spectra, the increasing number of looks result in reduction of MFPC. At lower frequencies, phase is closer to the real value that corresponds to the real height of the scene i.e. phase errors are lower. But at higher frequencies, phase fluctuations are higher and phase errors arise in random directions and averaging brings the phase close to 0, subsiding the higher frequencies in the phase frequency response. The MFPC are marked with black circles for the corresponding looks.
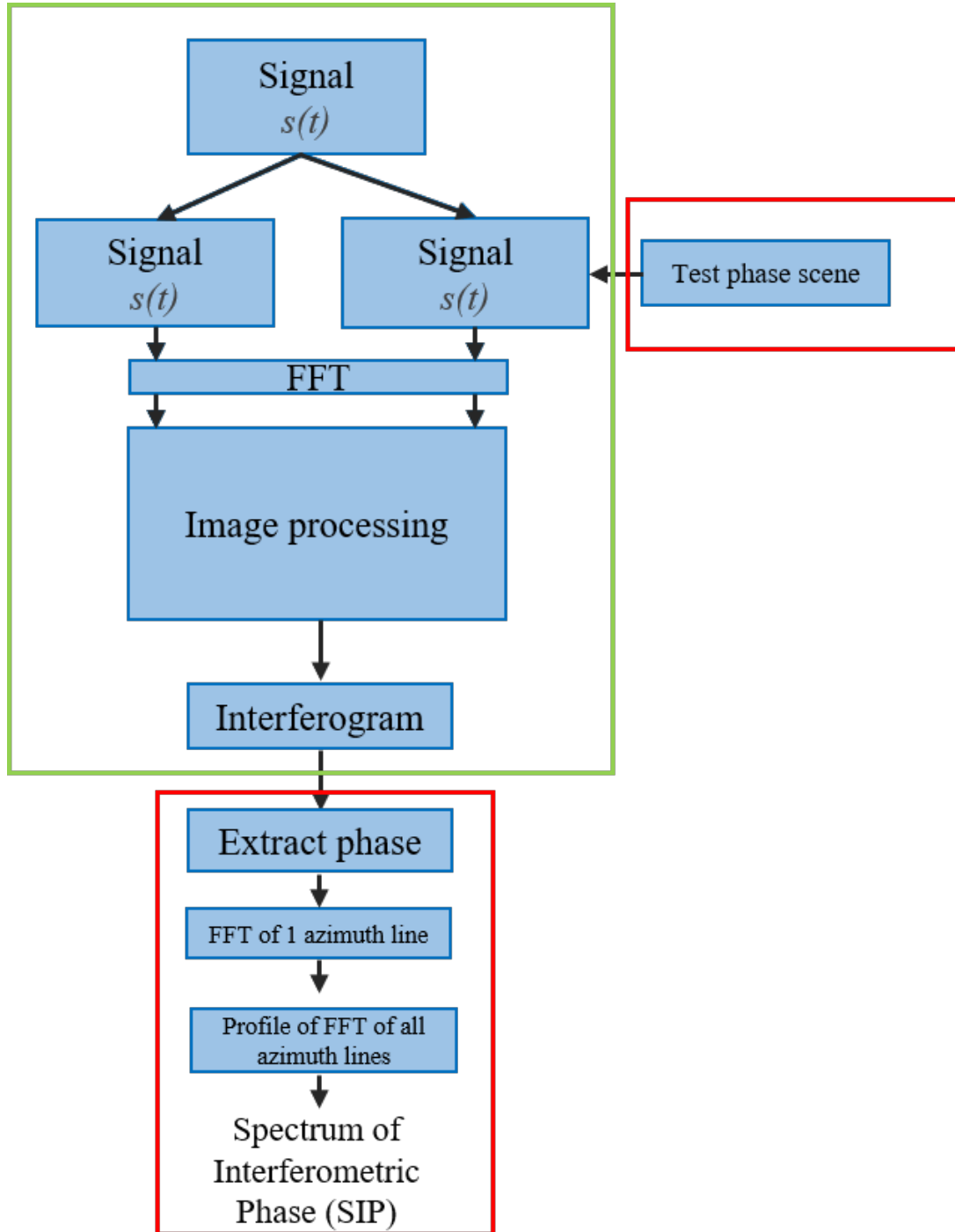
Fig. 5.9: Modification in the image processing steps involving the test phase scene to obtain spectrum of interferometric phase.
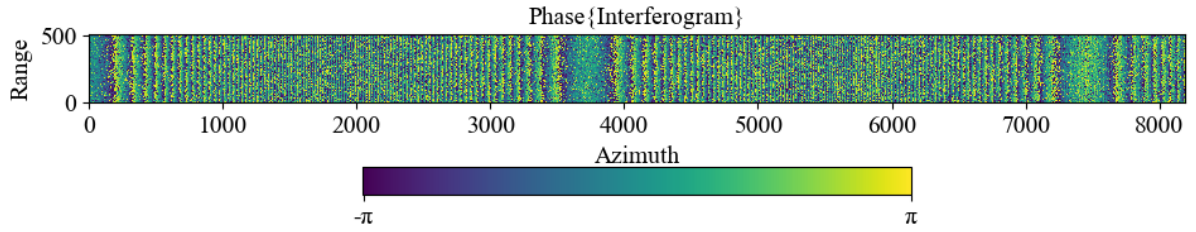
Fig. 5.10: Interferometric phase influenced by the test phase scene without antenna pattern correction performed on the complex image spectra.
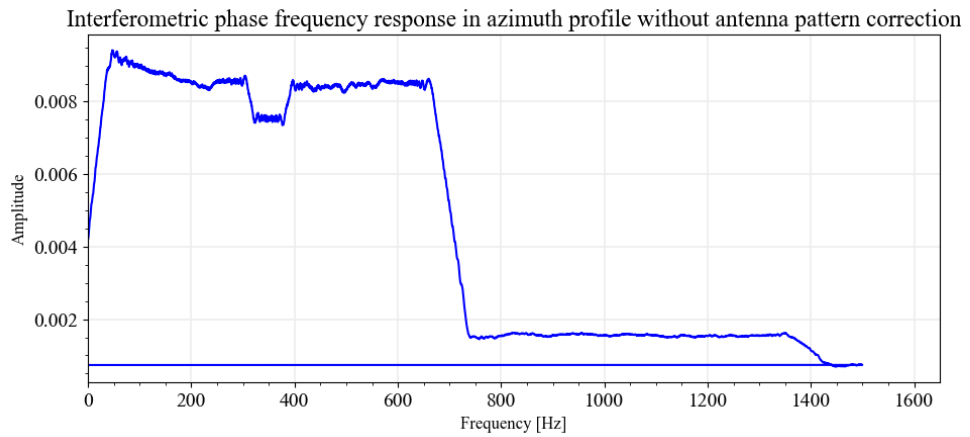
Fig. 5.11: SIP in azimuth profile without antenna pattern correction.
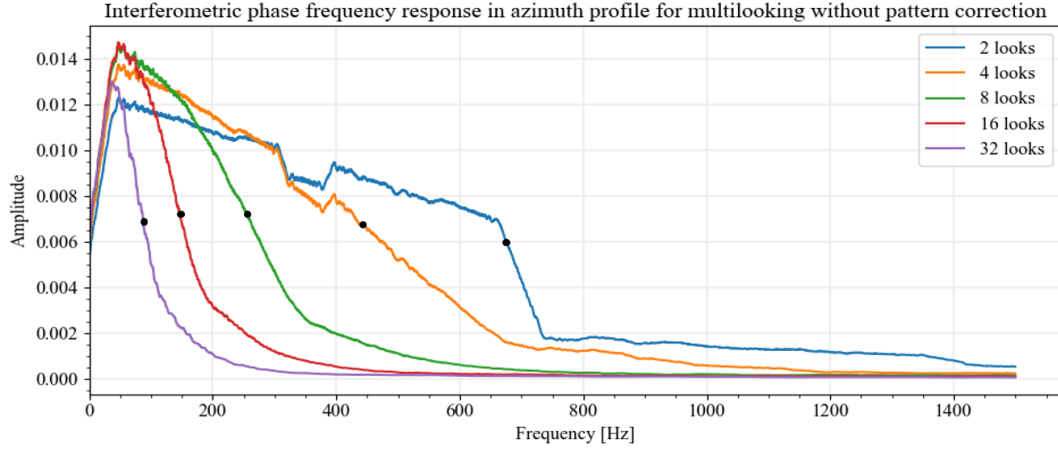
Fig. 5.12: Multilook performance of SIP with the influence of phase scene without antenna pattern correction on the spectrum.
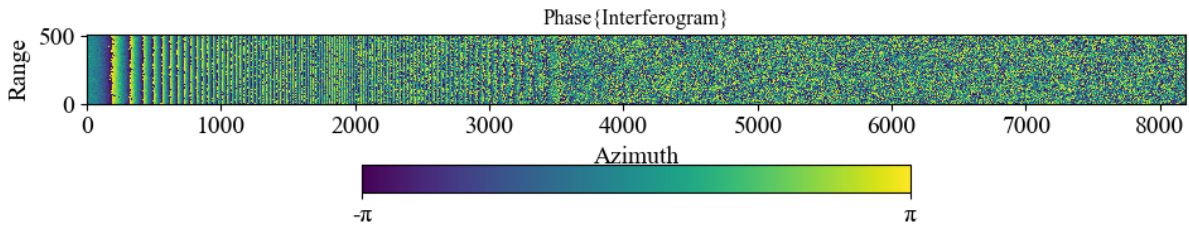
Fig. 5.13: Interferometric phase map for multilooking with 8 looks without antenna pattern correction.

(a) Interferometric phase in azimuth profile

(b) Interferometric phase in 1 azimuth line

Fig. 5.14: Spectrogram of the interferometric phase

In spatial domain, the moving average using a sequential/cascaded rectangular window is applied on the interferogram. Due to the effect of averaging, the higher rapid phase changes are subsided as was observed in multilook performance. The interferometric phase frequency response for different window sizes can be observed in Fig. 5.15. The MFPC is marked with black circles for the respective window sizes. Note that, the window size considered here is size of one rectangular window, and two such rectangular windows are cascaded, thus, the effective window size is twice of the mentioned size. On removal of the
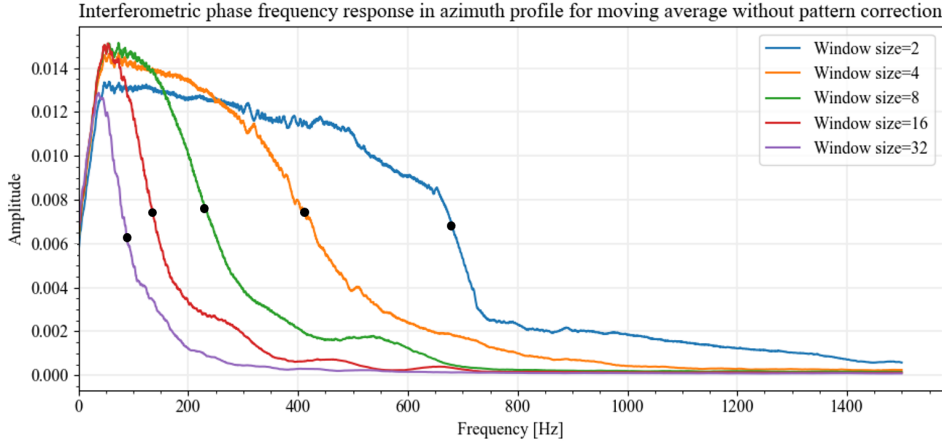
Fig. 5.15: SIP in azimuth profile for moving average with no antenna pattern correction.

phase scene from the interferogram, the interferometric phase only constitutes of phase errors. The standard deviations for the interferometric phase obtained by multilooking and moving average method have been used to compare the number of looks and size[3] of the window that result in the similar interferometric phase standard deviation σ and corresponding MFPC has been recorded in Tab. 5.9. For reference, the standard deviation is mentioned only for multilooking. The corresponding standard deviation for the moving average is recorded in Tab. 5.7.

Looks (K)	Window size in moving average (n)	σ [radians]	MFPC [Hz]	
			Multilooking	Moving average
1	1	0.965	700	700
2	2	0.642	672.8	678
4	4	0.381	433.5	415
8	8	0.229	251.7	230
16	16	0.152	143.4	135
32	32	0.104	86.8	87

Tab. 5.9: Number of looks and window size corresponding to MFPC for Case 1.

- **Case 2: With pattern correction:** In this case, the effect of antenna pattern has been corrected on the spectrum. Similar to Case 1, the averaging is carried out in spectral domain (multilooking) on the SAR image spectra and in the spatial domain the moving

---

[3]The effective window size of cascaded rectangular windows is 2n.

average has been made with a cascaded rectangular window on the interferogram. The interferometric phase spectrum in the azimuth profile without any averaging is depicted in Fig. 5.16. The maximum resolvable frequency of phase change is 700 Hz according to the phase scene. The same can be derived from the frequency response in this figure where the maximum observable frequency is 700 Hz corresponding to the phase amplitude of 0.00525.
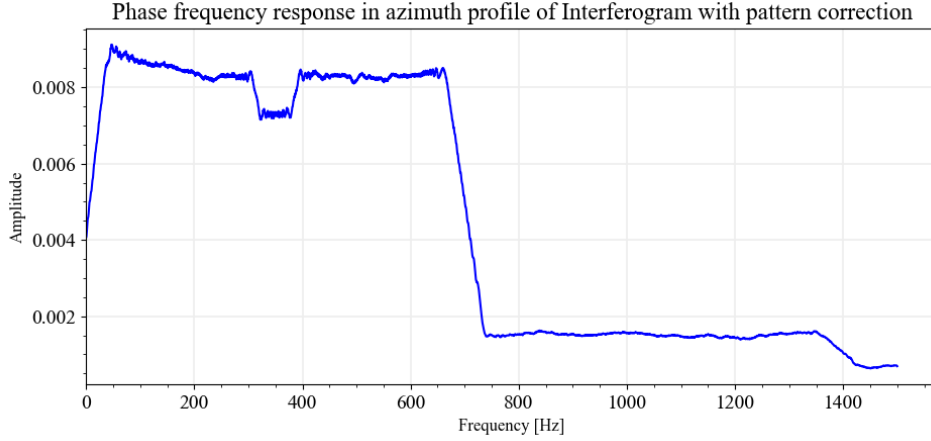
Fig. 5.16: SIP in azimuth profile with antenna pattern correction.

When averaging is performed in the spatial and spectral domain, the amplitude of the higher frequencies of phase change is reduced close to 0 value. This is expected as was observed in Case 1. As discussed earlier, the breakdown of frequencies is caused by the higher frequency of phase changes that are affected by the noise more adversely than the phase changes at lower frequencies. In Fig. 5.17, the maximum resolvable frequency of phase change can be observed for 8 looks in the phase map of the interferogram for multilooking. Fig 5.18 compares the performance results for multilook method and moving average method to observe maximum resolvable frequency of interferometric phase change for different degrees of looking and window sizes. The standard deviations for the interferometric phase are

Looks (K)	Window size in moving average (n)	σ [radians]	MFPC [Hz]	
			Multilooking	Moving average
1	1	1.01	700	700
2	2	0.694	674.7	683
4	4	0.42	435.4	413
8	8	0.254	254.5	228
16	16	0.168	142.4	131
32	32	0.116	88.7	85

Tab. 5.10: Number of looks and window size corresponding to maximum resolvable phase change frequency (MFPC) for Case 2.

obtained by removing the phase scene from the interferogram and after performing averaging by multilooking and moving average, the comparison has been made for the number of looks and size of the window that result in the similar interferometric phase standard deviation σ and corresponding MFPC has been recorded in Tab. 5.10. For reference, the standard
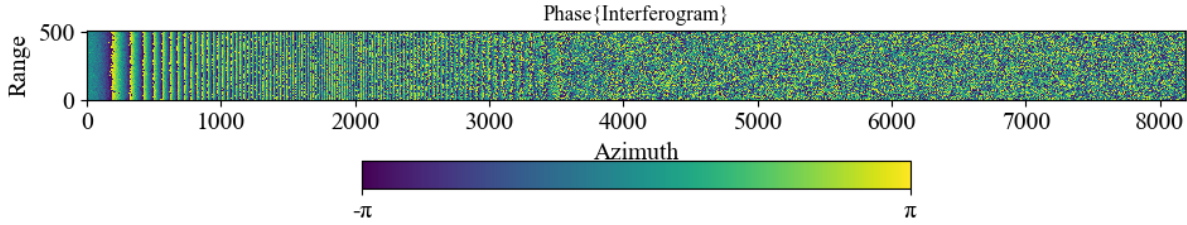
Fig. 5.17: Interferometric phase map for multilooking with 8 looks with antenna pattern correction.

deviation is mentioned only for multilooking. The corresponding standard deviation for the moving average is recorded in Tab. 5.8.

After obtaining these results, the curiosity arises for the performance in case of poor SNR. Let us consider an instance where the interferometric processing has been performed in presence of different noise levels, considering antenna pattern correction on the image spectra as shown in Fig. 5.19. The MFPC for different levels of SNR is marked with black circles.

For different SNR levels, it was observed that MFPC does not change considerably with decreasing SNR. For further assessment, the evaluation was extended for moving average performance with window size=8 and different SNR levels in the interferometric SAR pair spectra. The simulation results are depicted in Fig. 5.20. Black circles represent the MFPC for the respective SNR level. In this case, it was observed that the MFPC decreases with the decrease in the SNR. But the decrease is not significant enough to be compared to the noise levels. Also, the noise degrades the phase at lower frequencies as can been seen from the figure. This should further be investigated for varying interferometric processing parameters.
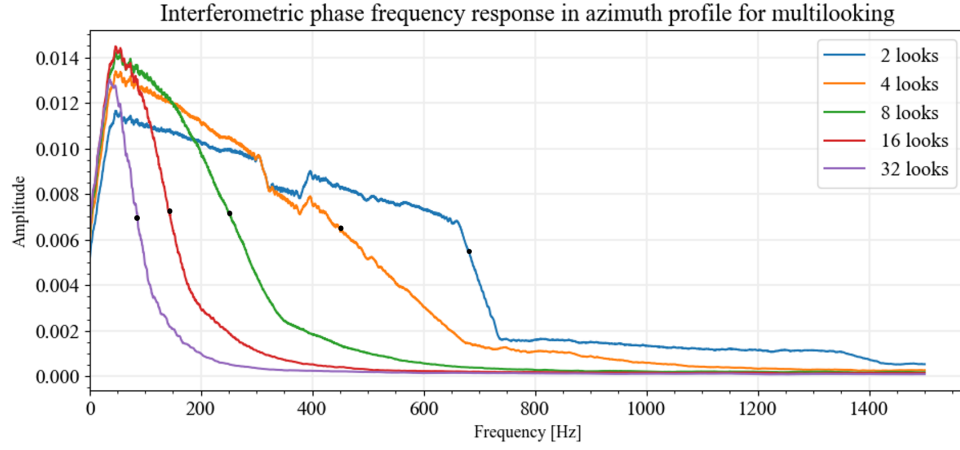
(a) Frequency response for multilooking
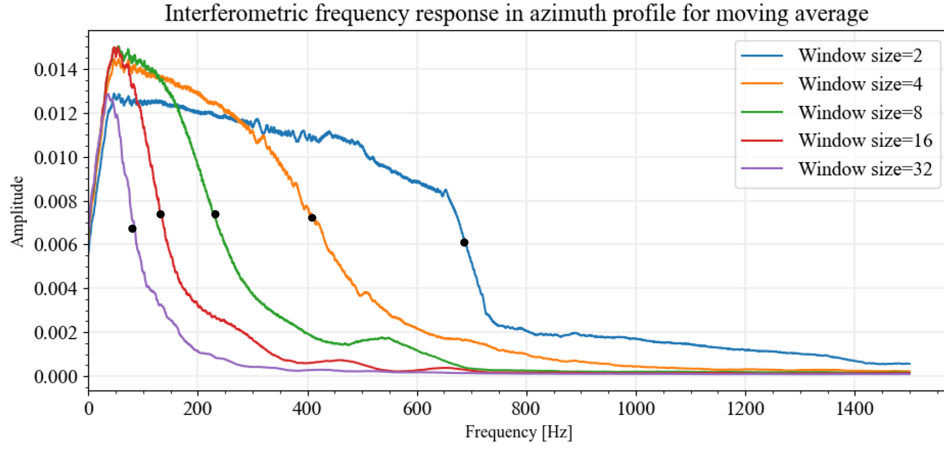
(b) Frequency response for moving average

Fig. 5.18: SIP in azimuth profile with antenna pattern correction.
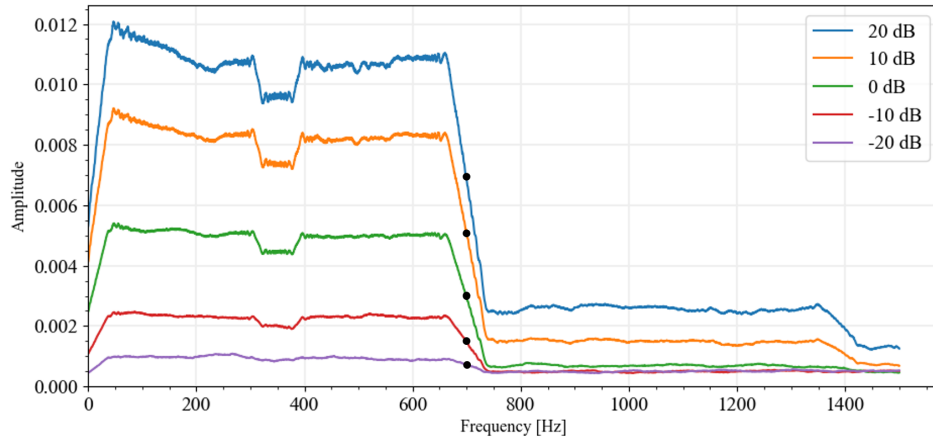
Fig. 5.19: SIP for different levels of SNR present in the SAR image pair for antenna pattern correction case.
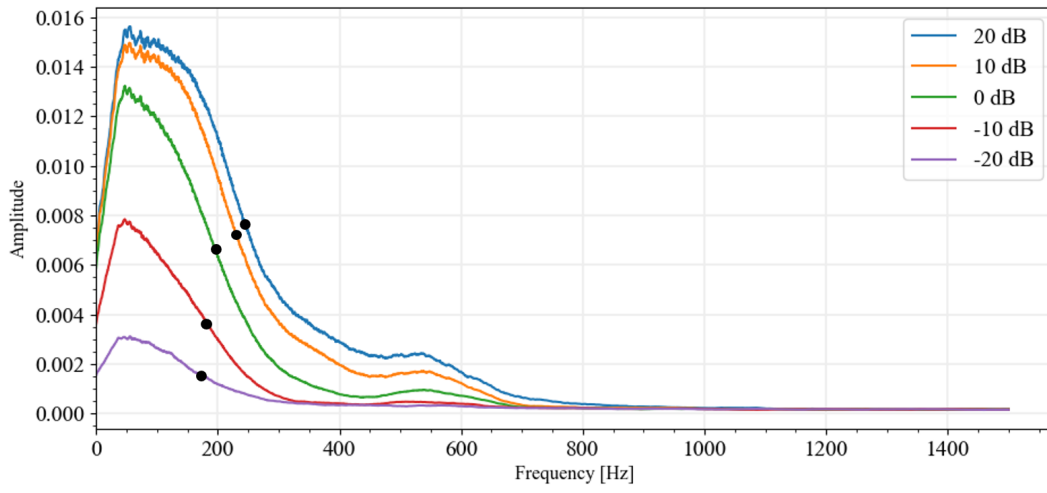
Fig. 5.20: SIP for different levels of SNR present in the SAR image pair for moving average with window size=8.

6 Summary

SAR Interferometry is a useful technique for the study of Earth topography, especially the construction of a Digital Elevation Model (DEM) for which the height measurement is directly related to the interferometric phase. The height accuracy is determined by the interferometric phase noise, which mainly is caused by Signal to Noise Ratio (SNR). Therefore, it is highly important to control the height accuracy by the employment of interferometric phase error reduction methods. This work presents a detailed overview of the SAR image processing and interferometric processing with the analysis of the influence of antenna radiation pattern on the image spectra and the interferometric phase errors that were measured and compared with the analytical predictions. The phase error reduction based on Multilooking involves the division of SAR interferometric image pair spectra into multiple sub-spectra called looks that are used to produce corresponding independent interferograms. The coherent addition of these interferograms reduces the phase errors. It was concluded from the performance results that a higher number of looks result in lower standard deviations of the interferometric phase. The other method based on moving average is applied on the interferogram for pixel-by-pixel error averaging, and it was shown that larger window sizes reduce the interferometric phase errors, but at the cost of resolution. These are the state-of-the-art methods that are applied in SAR interferometry. However, for interferograms, these error reduction methods were up-to-now analyzed in terms of phase differences that correspond to height difference measurement and height error. The ability to measure up to what maximum phase variations can be measured in a scene has not been explicitly described up to now. Therefore, in this work, a new concept has been developed that measures the maximum detectable frequency of phase change *MFPC*.

6.1 Key Observations and Discussion

Firstly, in this thesis, the influence of antenna pattern and its correction on the interferometric SAR image pair spectra were analyzed. It is known that if antenna pattern correction is not performed on the SAR image spectra, then weighting of the independent looks spectra is different due to the spectral weighting. In this case, it is difficult to define for each look the Impulse Response Function and geometric resolution. Hence, for image processing, antenna pattern correction is crucial for well-defined resolution. However, from simulation results involving a constant phase in the SAR interferometric image pair, it was concluded that the antenna pattern correction leads to an increase in phase noise in the outer spectra of the SAR image. Thus, for interferometric performance, the height measurement accuracy is degraded. Comprehensive simulations were carried out and presented to evaluate the interferometric phase error reduction performance of both methods i.e. multilooking in the image domain and moving average in the spatial domain. A correspondence has been found between the number of looks and the window size[4] of a cascaded rectangular sliding window used for moving average that results in the similar phase error standard deviations as can be observed from the tables below. Tab 6.1 and 6.2, show the correspondence for the SAR image pair spectra without antenna pattern

---

[4]The effective window size of the cascaded rectangular windows is 2n.

correction and with antenna pattern correction respectively. However, it is difficult to say if

Looks (K)	Window size in moving average (n)	σ [radians]	
		Multilooking	Moving average
1	1	0.965	0.965
2	2	0.642	0.642
4	4	0.381	0.389
8	8	0.229	0.231
16	16	0.152	0.156
32	32	0.104	0.111

Tab. 6.1: Number of looks and window size corresponding to similar phase standard deviations without antenna pattern correction.

Looks (K)	Window size in moving average (n)	σ [radians]	
		Multilooking	Moving average
1	1	1.01	1.01
2	2	0.694	0.691
4	4	0.42	0.421
8	8	0.254	0.236
16	16	0.168	0.157
32	32	0.116	0.108

Tab. 6.2: Number of looks and window size corresponding to similar phase standard deviations with antenna pattern correction.

this correspondence holds valid for practical cases as the performance is dependent on SNR, the shape of antenna pattern, and PRF. Additionally, it was observed that multilooking takes longer computation time as compared to doing moving average. Based on the correspondence, it can be concluded that for the similar error reduction results, moving average is a better processing method based on computational value. Furthermore, since moving average is directly applied on the interferogram, it can be used for error reduction regardless of the antenna pattern shape which is not a preferable solution with multilooking as the non-uniform weighting of the looks spectra destroys the impulse response function.

Secondly, in variations of the characteristics, this work concluded with the development of a very interesting preliminary concept of maximum phase change detection frequency. In the case of high phase variations in the interferogram, that were simulated using a test scene involving linearly increasing frequency of phase change, it was observed that for low noise levels i.e better SNR, the MFPC can be predicted analytically based on the type of window being used for averaging using 50% decay in the phase spectrum amplitude. In principle, it means that the MFPC is influenced by geometric resolution determined by the window. Based on the simulation results, it was concluded that error reduction methods improve interferometric performance but on the other hand deteriorate the resolution of MFPC in presence of rapid phase variations. This brings the work closer to a practical approach to interferometric processing. For high noise levels, it would be difficult to make analytical estimations and deeper investigation would be required. To throw light upon the same, brief analysis was made for different SNR levels in SAR image processing. In the interferometric processing, for the phase error reduction performance, it was observed that MFPC is reduced for a lower SNR but not to a large extent.

In conclusion, phase errors are the foremost important determinant of the quality of an iterferogram and spectral and spatial averaging methods prove to be legitimate phase error reduction techniques supported by measurements. In addition to it, the determinant MFPC is a promising quality indicator that addresses the conundrum of phase variations in an interferogram. This thesis lays a foundational ground work for the future prospect of this new entity.

6.2 Future Scope

This work presents preliminary development of the concept of MFPC. The work can be extended for the simulations on the real data to yield analytical derivations of the maximum detectable frequency of phase change that could be a measure for the choice of the window to be used in averaging. A myriad of possibilities beget from the concept that can further improve the quality of an interferogram and even better DEM could be obtained. Besides, the MFPC needs to be assessed further for different degrees of noise in the SAR images.

List of Figures

List of Tables

Bibliography

[1] G. Born, J. Dunne, and D. Lame, "Seasat mission overview," *Science*, vol. 204, no. 4400, pp. 1405–1406, 1979.

[2] I. G. Cumming and F. H. Wong, "Digital processing of synthetic aperture radar data," *Artech house*, vol. 1, no. 3, pp. 108–110, 2005.

[3] A. Moreira, P. Prats-Iraola, M. Younis, G. Krieger, I. Hajnsek, and K. P. Papathanassiou, "A tutorial on synthetic aperture radar," *IEEE Geoscience and Remote Sensing Magazine*, vol. 1, no. 1, pp. 6–43, 2013.

[4] P. Rizzoli and B. Bräutigam, "Radar backscatter modeling based on global tandem-x mission data," *IEEE Transactions on Geoscience and Remote Sensing*, vol. 52, 09 2014.

[5] Wikipedia, "Chirp — wikipedia, die freie enzyklopädie," 2021, [Online; Stand 1. Oktober 2022]. [Online]. Available: https://de.wikipedia.org/w/index.php?title=Chirp&oldid=214948656

[6] R. Bamler, "Principles of synthetic aperture radar," *Surveys in Geophysics*, vol. 21, no. 2, pp. 147–157, 2000.

[7] Z.-X. Zhou, Y. Deng, and R. Wang, "An innovative spaceborne sar concept with low prf: Using intra-pulse doppler effects for doppler spectrum recovery," in *EUSAR 2021; 13th European Conference on Synthetic Aperture Radar*. VDE, 2021, pp. 1–5.

[8] J. Curlander, "Geometric and rediametric distortion in spaceborne sar imagery," in *Proc. of the NASA Workshop on Registration and Rectification*, 1982.

[9] M. Tello, P. Lopez Dekker, and J. Mallorqui, "A novel strategy for radar imaging based on compressive sensing," *IEEE Transactions on Geoscience and Remote Sensing*, vol. 48, pp. 4285–4295, 01 2011.

[10] J. Gao, X. Xu, and F. Su, "Range cell migration of sar moving target based on envelope correlation method," in *2017 First International Conference on Electronics Instrumentation & Information Systems (EIIS)*. IEEE, 2017, pp. 1–5.

[11] E. MATLAB, "Sar image formation: Ers sar processor coded in matlab."

[12] R. Romeiser, M. Schwäbisch, J. Schulz-Stellenfleth, D. Thompson, R. Siegmund, A. Niedermeier, W. Alphers, and S. Lehner, "Study on concepts for radar interferometry from satellites for ocean (and land) applications," *Final Report(http://www. ifm. unihamburg. de/~ romeiser/koriolis. htm), University of Hamburg*, 2002.

[13] S. Blanchard, D. Rousseau, D. Gindre, and F. Chapeau-Blondeau, "Benefits from a speckle noise family on a coherent imaging transmission," *Optics Communications*, vol. 281, no. 17, pp. 4173–4179, 2008.

[14] P. Singh and R. Shree, "Analysis and effects of speckle noise in sar images," in *2016 2nd International Conference on Advances in Computing, Communication, & Automation (ICACCA) (Fall)*, 2016, pp. 1–5.

[15] J. P. Laboratory/NASA, "Pia01763: Space radar image of kilauea, hawaii - interferometry 1," 1999, [Online; Stand 1. Oktober 2022]. [Online]. Available: https://photojournal.jpl.nasa.gov/catalog/PIA01763

[16] JPL/NASA, "Pia01762: Space radar image of kilauea, hawaii," 1999, [Online; Stand 1. Oktober 2022]. [Online]. Available: https://photojournal.jpl.nasa.gov/catalog/PIA01763

[17] R. Bamler and P. Hartl, "Synthetic aperture radar interferometry," *Inverse problems*, vol. 14, no. 4, p. R1, 1998.

[18] D. Massonnet and T. Rabaute, "Radar interferometry: limits and potential," *IEEE Transactions on Geoscience and Remote Sensing*, vol. 31, no. 2, pp. 455–464, 1993.

[19] R. Kwok and M. Fahnestock, "Ice sheet motion and topography from radar interferometry," *IEEE Transactions on Geoscience and Remote Sensing*, vol. 34, no. 1, pp. 189–200, 1996.

[20] R. M. Goldstein, H. Engelhardt, B. Kamb, and R. M. Frolich, "Satellite radar interferometry for monitoring ice sheet motion: application to an antarctic ice stream," *Science*, vol. 262, no. 5139, pp. 1525–1530, 1993.

[21] J.-S. Lee, S. Cloude, K. Papathanassiou, M. Grunes, and I. Woodhouse, "Speckle filtering and coherence estimation of polarimetric sar interferometry data for forest applications," *IEEE Transactions on Geoscience and Remote Sensing*, vol. 41, no. 10, pp. 2254–2263, 2003.

[22] R. Romeiser, H. Runge, S. Suchandt, J. Sprenger, H. Weilbeer, A. Sohrmann, and D. Stammer, "Current measurements in rivers by spaceborne along-track insar," *IEEE Transactions on Geoscience and Remote Sensing*, vol. 45, no. 12, pp. 4019–4031, 2007.

[23] J. Bamber, J.-P. Muller, and A. Manganayake, "A global 5 arc minute digital elevation model derived from the geodetic phase of ers-1 (dem)," in *Third ERS Symposium on Space at the service of our Environment*, vol. 414, 1997, p. 1779.

[24] W. Alpers, H. Wang-Chen, and L. Hock, "Observation of internal waves in the andaman sea by ers sar," in *IGARSS'97. 1997 IEEE International Geoscience and Remote Sensing Symposium Proceedings. Remote Sensing - A Scientific Vision for Sustainable Development*, vol. 4, 1997, pp. 1518–1520 vol.4.

[25] Y. Xue, S. P. Lawrence, and D. T. Llewellyn-Jones, "Use of atsr data to estimate surface fluxes over land and sea," *ESA SP (Print)*, pp. 791–794, 1997.

[26] G. Krieger, A. Moreira, H. Fiedler, I. Hajnsek, M. Werner, M. Younis, and M. Zink, "Tandem-x: A satellite formation for high-resolution sar interferometry," *IEEE Transactions on Geoscience and Remote Sensing*, vol. 45, no. 11, pp. 3317–3341, 2007.

[27] (2022) Copernicus sentinels help to put europe's heatwave into context. [Online]. Available: https://sentinels.copernicus.eu/web/success-stories

[28] T. R. Lauknes, "Long-term surface deformation mapping using small-baseline differential sar interferograms," 10 2022.

[29] S. Jawak, "A review on applications of imaging synthetic aperture radar with a special focus on cryospheric studies," *Advances in Remote Sensing*, vol. 4, pp. 163–175, 06 2015.

[30] G. Ferraioli, "Multichannel sar interferometry based on statistical signal processing," *Universita degli Studi di Napoli: Ph. D. Thesis*, 2008.

[31] J. Mittermayer, T. Kraus, P. López-Dekker, P. Prats-Iraola, G. Krieger, and A. Moreira, "Wrapped staring spotlight sar," *IEEE Transactions on Geoscience and Remote Sensing*, vol. 54, no. 10, pp. 5745–5764, 2016.

[32] H. A. Zebker, J. Villasenor *et al.*, "Decorrelation in interferometric radar echoes," *IEEE Transactions on geoscience and remote sensing*, vol. 30, no. 5, pp. 950–959, 1992.

[33] R. Bamler, "Interferometric stereo radargrammetry: Absolute height determination from ers-envisat interferograms," in *IGARSS 2000. IEEE 2000 International Geoscience and Remote Sensing Symposium. Taking the Pulse of the Planet: The Role of Remote Sensing in Managing the Environment. Proceedings (Cat. No. 00CH37120)*, vol. 2.   IEEE, 2000, pp. 742–745.

[34] J. Mittermayer, G. Krieger, A. Bojarski, M. Zonno, M. Villano, M. Pinheiro, M. Bachmann, S. Buckreuss, and A. Moreira, "Mirrorsar: An hrws add-on for single-pass multi-baseline sar interferometry," *IEEE Transactions on Geoscience and Remote Sensing*, vol. 60, pp. 1–18, 2021.

[35] C. Lopez-Martinez and X. Fabregas, "Modeling and reduction of sar interferometric phase noise in the wavelet domain," *IEEE Transactions on Geoscience and Remote Sensing*, vol. 40, no. 12, pp. 2553–2566, 2002.

[36] L. Joughin and D. Winebrenner, "Effective number of looks for a multilook interferometric phase distribution," in *Proceedings of IGARSS'94-1994 IEEE International Geoscience and Remote Sensing Symposium*, vol. 4.   IEEE, 1994, pp. 2276–2278.

[37] Z. Yanjie and V. Prinet, "Insar coherence estimation," 01 2004.

[38] G. Schwarz, D. Espinoza-Molina, H. Breit, and M. Datcu, "Optimal multilooking for robust sar image indexing," 07 2008.

[39] A. Moreira, "Improved multilook techniques applied to sar and scansar imagery," *IEEE Transactions on geoscience and remote sensing*, vol. 29, no. 4, pp. 529–534, 1991.

[40] T. Kling and J. Kidwell, "Algorithms for reducing noise in synthetic aperture radar images," 2015.

[41] V. Mathuranathan and M. Viswanathan, *Digital Modulations Using Matlab: Build Simulation Models from Scratch.*   Independently Published, 2017. [Online]. Available: https://books.google.de/books?id=gCTjtAEACAAJ

[42] K. Tomiyasu, "Tutorial review of synthetic-aperture radar (sar) with applications to imaging of the ocean surface," *Proceedings of the IEEE*, vol. 66, no. 5, pp. 563–583, 1978.

[43] M. Bhanumurthy and Y. M. Reddy, "Sar data processing with range cell migration," *International Journal of Engineering Science and Technology*, vol. 3, no. 1, 2011.

[44] Y. Dukhopelnikova, "Methods of phase unwrapping in sar interferometry," in *The Fifth International Kharkov Symposium on Physics and Engineering of Microwaves, Millimeter, and Submillimeter Waves (IEEE Cat. No. 04EX828)*, vol. 1.   IEEE, 2004, pp. 226–228.

[45] R. M. Goldstein, H. A. Zebker, and C. L. Werner, "Satellite radar interferometry: Two-dimensional phase unwrapping," *Radio science*, vol. 23, no. 4, pp. 713–720, 1988.

[46] J. Strand, T. Taxt, and A. Jain, "Two-dimensional phase unwrapping using a block least-squares method," *IEEE Transactions on Image Processing*, vol. 8, no. 3, pp. 375–386, 1999.

[47] S. Dey, *Hands-On Image Processing with Python: Expert techniques for advanced image analysis and effective interpretation of image data*.   Packt Publishing Ltd, 2018.

[48] S. A. Khoshnevis and S. Ghorshi, "A tutorial on tomographic synthetic aperture radar methods," *SN Applied Sciences*, vol. 2, 09 2020.